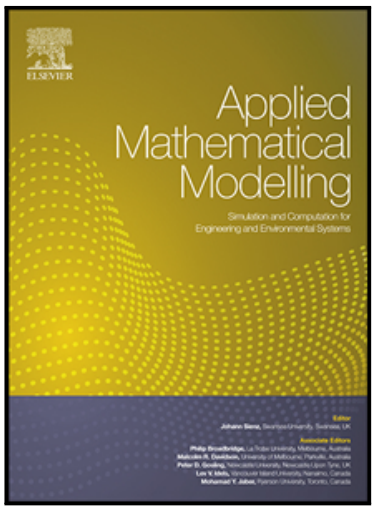

Modeling of both tensional-shear and compressive-shear fractures by a unified phase-field model

Qiao Wang , Qiang Yue , Wei Zhou , Y.T. Feng , Xiaolin Chang

PII: S0307-904X(22)00590-X
DOI: https://doi.org/10.1016/j.apm.2022.12.006
Reference: APM 14820

To appear in: *Applied Mathematical Modelling*

Received date: 20 May 2021
Revised date: 3 November 2022
Accepted date: 6 December 2022

Please cite this article as: Qiao Wang , Qiang Yue , Wei Zhou , Y.T. Feng , Xiaolin Chang , Modeling of both tensional-shear and compressive-shear fractures by a unified phase-field model, *Applied Mathematical Modelling* (2022), doi: https://doi.org/10.1016/j.apm.2022.12.006

Modeling of both tensional-shear and compressive-shear fractures by a unified phase-field model

Qiao Wang[1,2], Qiang Yue[1,2], Wei Zhou[1,2*], Y.T. Feng[3], Xiaolin Chang[1,2,*]

[1]*State Key Laboratory of Water Resources and Hydropower Engineering Science, Wuhan University, Wuhan 430072, China*

[2]*Institute of Water Engineering Sciences, Wuhan University, Wuhan 430072, China*

[3]*Zienkiewicz Centre for Computational Engineering, Swansea University, UK*

***Corresponding Author:**

Wei Zhou

State Key Laboratory of Water Resources and Hydropower Engineering Science

Wuhan University

Wuhan 430072, China

P.R. China

Email: zw_mxx@whu.edu.cn

***Corresponding Author:**

Xiaolin Chang

State Key Laboratory of Water Resources and Hydropower Engineering Science

Wuhan University

Wuhan 430072, China

P.R. China

Email: changxl@whu.edu.cn

Highlights

- A unified phase-field model for both tensional-shear and compressive-shear fractures is proposed.
- The failure compression strength is introduced to consider the fracture under compressive stress state.
- The crack angle can be determined by a universal fracture criterion easily.
- The proposed model can be applied for fracture in rock-like materials under complex stress states.

Abstract

Many phase-field models have been developed in recent years to captue different fracture modes from tensional to shear, tensional-shear, and compressive-shear fractures. However, there seems no phase-field model that can simulate the tensional, shear, tensional-shear, and compressive-shear fractures at the same time under complex stress states. In this paper, a unified phase-field model is proposed in the framework of the original phase-field theory. A universal fracture criterion, that can predict both tensional-shear and compressive-shear fractures under complex stress states is embedded in the proposed phase-field, and the failure compression strength is introduced to consider the fracture under a compressive stress state. Therefore, the crack direction can be directly determined from the universal fracture criterion. The strain energy of undamaged configuration is decomposed into three parts, the tensional/compressive part, the shear part, and the rest part. The tensional/compressive and shear parts can be degraded by different degradation functions or the same degradation function. Cohesive fracture models with general softening laws and the classical brittle fracture model can be used in the proposed model, and the length scale has much less influence on the global response if cohesive fracture models with general softening laws are applied. Numerical examples show that the proposed model has the ability to simulate both the tensional-shear and compressive-shear fractures in rock-like materials and the results are in good agreement with the experiments.

Keywords: phase-field model; tensional-shear and compressive-shear fractures; unified phase-field theory; universal fracture criterion; complex stress states.

1. Introduction

Material fracture or damage is one of the main causes of the failure of a structure in engineering. Many physical experiments have been conducted to figure out the fracture behaviors

of different materials, such as glass [1], metal [2], ice [3], concrete [4], rock [5] and so on. Numerical methods have also been developed to model fracture problems since they can easily consider different material properties, complex structure shapes, and various boundary conditions. These numerical methods include the boundary element method [6-8], the extended finite element method [9, 10], the meshfree methods [11], the peridynamics [12-14], the cracking particle method [15, 16], the screened Poisson equation [17, 18], the cellular automaton method [19, 20] and the phase-field model [21-24].

The phase-field model has become one of the most popular methods for modeling crack propagation in recent years. The key idea of the phase-field model is treating the cracked domain as a multi-phase system by introducing a phase-field variable $s \in [0,1]$, where s=0 and s=1 represent two distinct phases of intact solid and crack respectively, while $0<s<1$ for a damaged region call the interface. Thus, a crack set, i.e., the sharp-interfaces are regarded as diffuse-interfaces, which can eliminate the singularity and discontinuity caused by the sharp-interfaces and can be implemented in numerical methods much easier. Then crack paths or damaged areas can be automatically tracked by the value of the phase-field variable s over the domain. Usually, a diffusion equation is introduced to track the phase evolution over time.

Several phase-field models were developed both in physics communities [25-30] and mechanics communities [31-34] and have been applied in many areas [21, 35-45]. In phase-field models, the phase-field and the displacement field are connected by a degradation function with respect to the phase-field variable, and the energy of the solid will be degraded by the degradation function. Therefore, the degradation function usually takes a value between 0 and 1. In the original phase-field model, the (degraded) energy density function was evaluated simply by multiplying the strain energy of undamaged configuration with the degradation function [32]. Therefore, it cannot distinguish fracture behaviors between tension and compression [46].

Several efforts have been made to avoid material damage under the compressive state by decomposing the strain energy of undamaged configuration into two parts, the tensional part and the compressive part; and only the tensional part is multiplied by the degradation function. For example, Amor et al. [31] decomposed the elastic energy density into volumetric and deviatoric parts. Miehe et al. [47, 48] applied the spectral decomposition of the strain tensor to split the energy into the tensile part and the compressive part. Wu et al. [49] proposed a variationally consistent phase-field based on the positive/negative projection of the effective stress [50]. Steinke

et al. [51] proposed a phase-field model based on the directional stress decomposition. In order to simulate the fracture behavior of rock-like materials under compression, Zhang et al. [52] proposed a modified phase-field model by splitting the tensile part in the spectral decomposition [47, 48] into a mode-I component and a shearing component based on the modified G-criterion [53]. Bryant and Sun [54] presented a mixed-mode phase-field fracture model in anisotropic rocks with consistent kinematics. Recently, Wang et al. [55] proposed a new mixed phase-field model based on a unified tensile fracture criterion, and it can be applied not only to tensional-shear fracture but also to shear fracture under compression for rock-like materials. However, although some of these models can simulate fracture behaviors under compression, few compressive-shear fracture was considered.

To consider compressive-shear fracture, some researchers have tried to couple the well-known criterion for rock-like materials in the phase-field model. Zhou et al. [56] constructed a new driving force in the evolution equation of the phase-field model by considering the influence of the cohesion and the internal friction angle. Wang et al. [57] derived the driving force in the phase-field model based on the Mohr-Coulomb criterion with shear frictional characteristics. Though these models can consider the compressive-shear fracture very well in rock-like materials, they cannot consider the tensional-shear fracture at the same time.

In this paper, a unified phase-field model is developed for both tensional-shear and compressive-shear fractures. The proposed model is derived based on a universal fracture criterion [58] in the framework of the unified phase-field theory [59]. Within this criterion, the maximum normal stress criterion, the Tresca criterion, and the Mohr-Coulomb criterion are special cases [58]. The universal fracture criterion also has the ability to describe different fracture patterns under various external loading conditions [58], including the tensional fracture, shear fracture, tensional-shear fracture, and compressive-shear fracture. To consider the compressive-shear fracture, the failure compression strength of a material is introduced into the proposed phase-field model according to the universal fracture criterion. The strain energy of undamaged configuration computed from the effective stress [50] is decomposed into three parts: the tensional/compressive part, the shear part, and the rest. The tensional/compressive part and the shear part can be degraded by the same or different degradation functions. The crack direction can be determined from the universal fracture criterion directly. Cohesive fracture models with general softening laws and the classical brittle fracture model can be incorporated into the proposed model since it is

developed in the framework of the unified phase-field theory [59]. The length scale has much less influence on the global response if the cohesive fracture models with general softening laws are used. Compared with the mixed-mode phase-field model proposed by Wang et al. [55], only one additional material parameter, i.e., the failure compression strength, is needed. Numerical examples show that the proposed model can simulate both the tensional-shear fracture and compressive-shear fracture at the same time, and the crack paths are in good agreement with the experiments.

The paper is organized as follows. The governing equations and basic theory of the original unified phase-field theory are reviewed in Section 2. The unified phase-field model for both tensional-shear and compressive-shear fractures is proposed in Section 3, followed by analytical solutions for a 2D bar under uniaxial tension and compression in Section 4. In Section 5, the implementation of the proposed model within the finite element method is discussed and the numerical results are presented in Section 6. Conclusions are drawn in Section 7.

2. The basic theory of the original unified phase-field model

2.1 The governing equations for the phase-field model

Considering a bounded domain Ω with boundary $\partial\Omega = \partial\Omega_u \bigcup \partial\Omega_t$, in which $\partial\Omega_u$ and $\partial\Omega_t$ are the displacement and traction boundaries, respectively (see Figure 1(b)). Γ_c is a set of cracks in the domain (see Figure 1(a)). The sharp cracks Γ_c can be approximated as regularized cracks in the phase-field model by (see Figure 1(a))

$$\int_{\Gamma_c} \mathrm{d}\Gamma_c \approx \int_{\Omega} \gamma(s,\nabla s)\mathrm{d}\Omega \tag{1}$$

where $\gamma(s,\nabla s)$ is a crack surface density function and $s \in [0,1]$ is the phase-field variable.

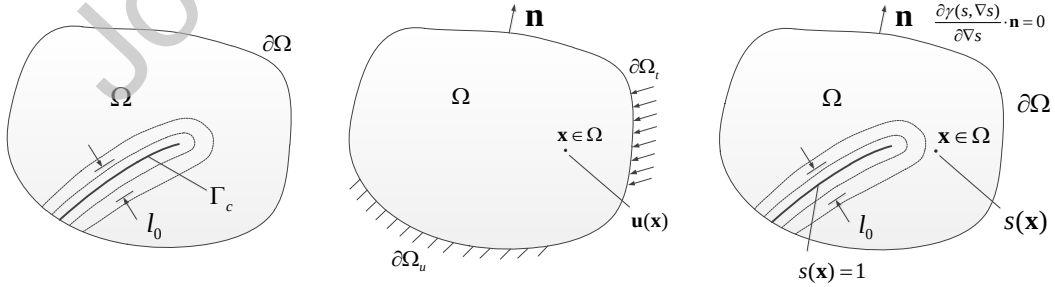

Figure 1. Phase-field model for crack embedded in the solid: (a) Sharp crack and regularized crack; (b) Boundary conditions for equilibrium equation; (c) Boundary conditions for evolution equation

The governing equations for the phase-field model can be obtained in different ways [34, 60] and in this paper, they are given as [22, 59]

Equilibrium equation:

$$\mathrm{div}\boldsymbol{\sigma}(\mathbf{u},s)=\mathbf{0} \tag{2}$$

and evolution equation:

$$\begin{cases} G_c\nabla\cdot(\dfrac{\partial\gamma(s,\nabla s)}{\partial\nabla s})-G_c\dfrac{\partial\gamma(s,\nabla s)}{\partial s}-\dfrac{\partial\psi(\boldsymbol{\varepsilon}(\mathbf{u}),s)}{\partial s}=0, & \delta s\geq 0 \\ G_c\nabla\cdot(\dfrac{\partial\gamma(s,\nabla s)}{\partial\nabla s})-G_c\dfrac{\partial\gamma(s,\nabla s)}{\partial s}-\dfrac{\partial\psi(\boldsymbol{\varepsilon}(\mathbf{u}),s)}{\partial s}\leq 0, & \delta s=0 \end{cases} \tag{3}$$

with the following boundary conditions (see Figure 1 (b) and Figure 1 (c))

$$\boldsymbol{\sigma}(\mathbf{u},s)\mathbf{n}=\bar{\mathbf{t}} \quad \text{on} \quad \partial\Omega_t \tag{4}$$

$$\frac{\partial\gamma(s,\nabla s)}{\partial\nabla s}\cdot\mathbf{n}=0 \quad \text{on} \quad \partial\Omega \tag{5}$$

where $\mathbf{u}$ is the displacement vector; $\boldsymbol{\sigma}$ is the stress tensor; $\boldsymbol{\varepsilon}$ is the strain tensor; $\bar{\mathbf{t}}$ is the prescribed surface traction; $\mathbf{n}$ is the unit outward normal of the boundary; G_c is the fracture toughness or energy [61]; and $\psi(\boldsymbol{\varepsilon},s)$ is the energy density function defined by

$$\psi(\boldsymbol{\varepsilon}(\mathbf{u}),s)=\omega(s)\psi_0(\boldsymbol{\varepsilon}(\mathbf{u})) \tag{6}$$

in which $\omega(s)$ is the degradation function and $\psi_0(\boldsymbol{\varepsilon}(\mathbf{u}))$ is the strain energy of undamaged configuration defined as

$$\psi_0=\frac{1}{2}\lambda\mathrm{tr}^2[\boldsymbol{\varepsilon}]+\mu\mathrm{tr}[\boldsymbol{\varepsilon}^2] \tag{7}$$

where λ and μ are the Lame constants.

In the phase-field model, the stress tensor $\boldsymbol{\sigma}(\mathbf{u},s)$ is determined by

$$\boldsymbol{\sigma}(\mathbf{u},s)=\frac{\partial\psi(\boldsymbol{\varepsilon}(\mathbf{u}),s)}{\partial\boldsymbol{\varepsilon}} \tag{8}$$

Different surface density functions $\gamma(s,\nabla s)$ and degradation functions $\omega(s)$ can lead to different phase-field models.

2.2 The surface density function

Without loss of generality, the generic form of the crack surface density function proposed in the unified phase-field theory [59] is considered as

$$\gamma(s,\nabla s)=\frac{1}{c_0}(\frac{1}{l_0}\alpha(s)+l_0|\nabla s|^2) \tag{9}$$

with

$$\alpha(s)=\xi_1 s+\xi_2 s^2+\cdots+\xi_m s^m,\qquad \sum_{i=1}^{m}\ \xi_i=1 \tag{10}$$

$$c_0=4\int_0^1\ \sqrt{\alpha(x)}\mathrm{d}x \tag{11}$$

where l_0 is an internal length scale regularizing the crack (Figure 1 (a)); and $\alpha(s)$, as a polynomial function of *s* with coefficients ξ_i, is called the geometric crack function and controls the distribution of the phase-field function $s(\mathbf{x})$ in the problem domain. Some commonly used functions $\alpha(s)$ and the corresponding $s(\mathbf{x})$ can be found in [36, 59, 60, 62-65]. In the unified phase-field theory [59], the following geometric crack function is used:

$$\alpha(s)=\xi s+(1-\xi)s^2 \tag{12}$$

and it suggests $\xi=2$. The solution for $\xi=0$ coupled with general softening laws is obtained in [66].

By using Equation (9), Equation (3) can be rewritten as

$$\frac{2G_c l_0}{c_0}\nabla^2 s-\frac{G_c}{c_0 l_0}\alpha'(s)-\omega'(s)\psi_0\le 0 \tag{13}$$

or

$$\omega'(s)\frac{\psi_0}{G_c}\ge\frac{2l_0}{c_0}\nabla^2 s-\frac{\alpha'(s)}{c_0 l_0} \tag{14}$$

2.3 The degradation function

The degradation function $\omega(s)$ has a significant influence on the global response of the model and possesses the following properties [48]

$$\omega(0)=1,\qquad \omega(1)=0,\qquad \omega'(1)=0 \tag{15}$$

Many different degradation functions have been proposed and a list can be found in [22]. In the classical phase-field mode, the degradation function is expressed as $\omega(s)=(1-s)^2$.

In the unified phase-field theory, $\omega(s)$ can be defined as

$$\omega(s)=\frac{(1-s)^p}{(1-s)^p+Q(s)}=\frac{1}{1+\phi(s)},\qquad \phi(s)=\frac{Q(s)}{(1-s)^p} \tag{16}$$

where $p>0$, $Q(s)\ge 0$ and

$$Q(s)=a_1 s+a_1 a_2 s^2+a_1 a_2 a_3 s^3+a_1 a_2 a_3 a_4 s^4+\cdots \tag{17}$$

where a_i are parameters can be determined from the material properties and given softening

laws.

3. A unified phase-field model for tensional-shear and compressive-shear fractures

In this section, the phase-field model for both tensional-shear and compressive-shear fractures is introduced based on the universal failure criterion [58]. The proposed phase-field model is an extension of the phase-field model for tensional-shear fracture [55], thus, the model for tensional-shear fracture is introduced first.

3.1 The phase-field model for tensional-shear fracture [55]

To obtain the phase-field model for tensional-shear fracture, one can decompose the energy density into

$$\psi = \omega_I(s)\psi_{0I} + \omega_{II}(s)\psi_{0II} \tag{18}$$

where $\omega_I(s)$ and $\omega_{II}(s)$ are two degradation functions defined as

$$\omega_I(s) = \frac{1}{1+\phi_I(s)} = \frac{1}{1+b_I\phi(s)}, \qquad \omega_{II}(s) = \frac{1}{1+\phi_{II}(s)} = \frac{1}{1+b_{II}\phi(s)} \tag{19}$$

where b_I and b_{II} are two parameters.

Take the plane stress problem as an example, ψ_{0I} and ψ_{0II} can be defined as

$$\psi_{0I} = \frac{1}{2E}(\bar{\sigma}^{\mathbf{nn}})^2 + \frac{1}{2E}(\bar{\sigma}^{\mathbf{mm}})^2 - \frac{\nu}{E}\bar{\sigma}^{\mathbf{nn}}\bar{\sigma}^{\mathbf{mm}} \tag{20}$$

$$\psi_{0II} = \frac{1}{2\mu}(\bar{\sigma}^{\mathbf{nm}})^2 = \frac{1}{2\mu}\bar{\tau}^2 \tag{21}$$

where E is the elasticity modulus; $\bar{\sigma}^{\mathbf{nn}}$ and $\bar{\sigma}^{\mathbf{nm}} = \bar{\tau}$ are the effective normal stress and shear stress, respectively, and can be computed by

$$\bar{\sigma}^{\mathbf{nn}} = \bar{\boldsymbol{\sigma}} : \mathbf{M}^{\mathbf{nn}}, \bar{\sigma}^{\mathbf{nm}} = \bar{\boldsymbol{\sigma}} : \mathbf{M}^{\mathbf{nm}} \tag{22}$$

with

$$\mathbf{M}^{\mathbf{nn}} = \mathbf{n}\otimes\mathbf{n}, \mathbf{M}^{\mathbf{nm}} = \mathbf{n}\otimes\mathbf{m} \tag{23}$$

where the vector $\mathbf{n}$ is perpendicular to the crack surface, the vector $\mathbf{m}$ is parallel to the crack surface; and $\bar{\boldsymbol{\sigma}} = \boldsymbol{\Lambda}\boldsymbol{\varepsilon}$ is the effective stress tensor, where $\boldsymbol{\Lambda}$ is the standard elasticity tensor [49].

And the elasticity tensor is defined as [55]

$$\mathbb{D} = \omega_I(s)\frac{\partial}{\partial\boldsymbol{\varepsilon}}\frac{\partial(\psi_0 - \psi_{0II})}{\partial\boldsymbol{\varepsilon}} + \omega_{II}(s)\frac{\partial}{\partial\boldsymbol{\varepsilon}}\frac{\partial\psi_{0II}}{\partial\boldsymbol{\varepsilon}} \tag{24}$$

The stress tensor $\boldsymbol{\sigma}$ is defined as

$$\boldsymbol{\sigma} = \omega_I(s)\frac{\partial(\psi_0 - \psi_{0II})}{\partial \boldsymbol{\varepsilon}} + \omega_{II}(s)\frac{\partial \psi_{0II}}{\partial \boldsymbol{\varepsilon}} \tag{25}$$

The relationship between $\boldsymbol{\sigma}$ and $\bar{\boldsymbol{\sigma}}$ is replaced by

$$\begin{bmatrix} \sigma^{\mathbf{nn}} \\ \sigma^{\mathbf{mm}} \\ \sigma^{\mathbf{nm}} \end{bmatrix} = \begin{bmatrix} \omega_I(s) & 0 & 0 \\ 0 & \omega_I(s) & 0 \\ 0 & 0 & \omega_{II}(s) \end{bmatrix} \begin{bmatrix} \bar{\sigma}^{\mathbf{nn}} \\ \bar{\sigma}^{\mathbf{mm}} \\ \bar{\sigma}^{\mathbf{nm}} \end{bmatrix} \tag{26}$$

To obtain the evolution equation for tensional-shear fracture, one can refer to the modified G-criterion [53, 67]:

$$F(\theta) = \frac{G_I(\theta)}{G_{cI}} + \frac{G_{II}(\theta)}{G_{cII}} \tag{27}$$

where $F(\theta)$ is a parameter that controls the propagation of a crack tip, θ is the crack propagation direction, $G_I(\theta)$ and $G_{II}(\theta)$ are the mode I and mode II energy release rates, G_{cI} and G_{cII} are the fracture toughnesses for Mode-I and Mode-II fractures, respectively. Similar to Equation (27), Equation (14) can be rewritten as

$$\omega_I'(s)\frac{\psi_{0I}^+}{G_{cI}} + \omega_{II}'(s)\frac{\psi_{0II}}{G_{cII}} \geq \frac{2l_0}{c_0}\nabla^2 s - \frac{\alpha'(s)}{c_0 l_0} \tag{28}$$

Once G_{cI} and G_{cII} are known, Equation (28) can be solved to obtain the phase-field. It should be noted that ψ_{0I}^+ is used instead of ψ_{0I} to avoid the crack propagation under compressive stress [55] in Equation (28), and

$$\psi_{0I}^+ = \frac{1}{2E}\left\langle \bar{\sigma}^{\mathbf{nn}} \right\rangle_+^2 \tag{29}$$

where $\langle x \rangle_\pm = (x \pm |x|)/2$.

In this paper, we will use the following "ellipse criterion" (see Figure 2(a)) [68] instead of the G-criterion to consider the tensional-shear fracture

$$\frac{\sigma^2}{\sigma_t^2} + \frac{\tau^2}{\tau_s^2} = 1 \tag{30}$$

where σ_t and τ_s are the critical normal tensile fracture stress and critical shear failure stress, respectively. The connections between G_{cI} and σ_t, G_{cII} and τ_s can be obtained by considering the tensional fracture and shear fracture, respectively, i.e. [55]

$$G_{cI} = \frac{c_0 l_0 b_I}{2E} \frac{\phi'(0)}{\alpha'(0)} \sigma_t^2 \tag{31}$$

$$G_{cII} = \frac{c_0 l_0 b_{II}}{2\mu} \frac{\phi'(0)}{\alpha'(0)} \tau_s^2 = \chi^2 \frac{G_{cI} E b_{II}}{\mu b_I} \tag{32}$$

where $\chi = \tau_s / \sigma_t$ is a material parameter. One can further define the following fracture toughnesses as

$$\bar{G}_{cI} = \frac{G_{cI}}{b_I} = \frac{c_0 l_0}{2E} \frac{\phi'(0)}{\alpha'(0)} \sigma_t^2 \tag{33}$$

$$\bar{G}_{cII} = \frac{G_{cII}}{b_{II}} = \chi^2 \frac{\bar{G}_{cI} E}{\mu} \tag{34}$$

It can be noted that $\bar{G}_{cI}$ and $\bar{G}_{cII}$ are independent of the parameters b_I and b_{II}.

Substituting Equations (31) and (32) into Equation (28), one can obtain

$$\frac{\left\langle \bar{\sigma}^{\mathbf{nn}} \right\rangle_+^2}{\sigma_t^2} \frac{\omega_I'(s)}{\phi_I'(0)} + \frac{(\bar{\sigma}^{\mathbf{nm}})^2}{\tau_s^2} \frac{\omega_{II}'(s)}{\phi_{II}'(0)} \leq \frac{2l_0^2 \nabla^2 s - \alpha'(s)}{\alpha'(0)} \tag{35}$$

and

$$\frac{\left\langle \sigma^{\mathbf{nn}} \right\rangle_+^2}{\sigma_t^2} + \frac{(\sigma^{\mathbf{nm}})^2}{\tau_s^2} \leq -\frac{2l_0^2 \nabla^2 s - \alpha'(s)}{\alpha'(0)} \frac{\phi'(0)}{\phi'(s)} \tag{36}$$

which are similar to the "ellipse criterion" shown in Equation (30).

The elasticity tensor introduced in Equation (24) will lead to a non-linear system of equilibrium equation to be solved if $b_I \neq b_{II}$ and the resulting model can be called an anisotropic phase-field model.

Remark 3.1. If let $b_I = b_{II} = 1$, the stress tensor and elasticity tensor become

$$\begin{cases} \boldsymbol{\sigma} = \omega_I(s) \dfrac{\partial \psi_0}{\partial \boldsymbol{\varepsilon}} \\ \mathbb{D} = \omega_I(s) \dfrac{\partial}{\partial \boldsymbol{\varepsilon}} \dfrac{\partial \psi_0}{\partial \boldsymbol{\varepsilon}} \end{cases} \tag{37}$$

which can be considered a special model. In particular, a linear system of equations will be obtained while solving the equilibrium equation. It was found that this special model is much more efficient and it can obtain similar numerical results [55].

3.2 Phase-field model for both tensional-shear and compressive-shear fractures

The above model can only be applied in tensional-shear fracture, including pure tensional

and pure shear fractures, and the failure criterion is similar to the unified failure criterion [68]. However, the fracture under compressive stress can not be considered. In order to consider compressive-shear fracture, one can further apply the universal failure criterion as [58] (see Figure 2)

$$\beta\frac{\sigma^2}{\sigma_t^2}+\frac{\tau^2}{\tau_s^2}=1 \tag{38}$$

where $\beta=1$ for $\sigma_1+\sigma_2\geq 0$ and $\beta=\bar{\beta}$ for the case $\sigma_1+\sigma_2<0$ (σ_1 and σ_2 are the first and second principal stress). $\bar{\beta}$ is a material parameter needed to be calibrated for different materials [58] according to the compressive experiment. Then the decomposition of the energy density can be revised to

$$\psi=\beta\omega_I(s)\psi_{0I}+\omega_{II}(s)\psi_{0II}+\bar{\psi_0} \tag{39}$$

where

$$\bar{\psi_0}=\psi_0-\beta\psi_{0I}-\psi_{0II} \tag{40}$$

Consequently, Equation (35) and Equation (36) can be rewritten as

$$\beta\frac{(\bar{\sigma}^{\mathbf{nn}})^2}{\sigma_t^2}\frac{\omega_I'(s)}{\phi_I'(0)}+\frac{(\bar{\sigma}^{\mathbf{nm}})^2}{\tau_s^2}\frac{\omega_{II}'(s)}{\phi_{II}'(0)}\geq\frac{2l_0^2\nabla^2 s-\alpha'(s)}{\alpha'(0)} \tag{41}$$

$$\beta\frac{(\sigma^{\mathbf{nn}})^2}{\sigma_t^2}+\frac{(\sigma^{\mathbf{nm}})^2}{\tau_s^2}\leq-\frac{2l_0^2\nabla^2 s-\alpha'(s)}{\alpha'(0)}\frac{\phi'(0)}{\phi'(s)} \tag{42}$$

Equations (24) and (25) are still applicable in the compressive-shear fracture and the final formulations can be expressed as

$$\begin{cases}\begin{cases}\omega_I'(s)\beta\dfrac{\psi_{0I}}{G_{cI}}+\omega_{II}'(s)\dfrac{\psi_{0II}}{G_{cII}}\geq\dfrac{2l_0}{c_0}\nabla^2 s-\dfrac{\alpha'(s)}{c_0 l_0}\\ \psi_{0I}=\dfrac{1}{2E}(\bar{\sigma}^{\mathbf{nn}})^2,\psi_{0II}=\dfrac{1}{2\mu}(\bar{\sigma}^{\mathbf{nm}})^2\\ \bar{G}_{cI}=G_{cI}/b_I=\dfrac{c_0 l_0}{2E}\dfrac{\phi'(0)}{\alpha'(0)}\sigma_t^2,\bar{G}_{cII}=G_{cII}/b_{II}=\chi^2\dfrac{\bar{G}_{cI}E}{\mu}\end{cases}\\ \begin{cases}\mathrm{div}\boldsymbol{\sigma}=\mathbf{0}\\ \boldsymbol{\sigma}=\omega_I(s)\dfrac{\partial(\psi_0-\psi_{0II})}{\partial\boldsymbol{\varepsilon}}+\omega_{II}(s)\dfrac{\partial\psi_{0II}}{\partial\boldsymbol{\varepsilon}}\\ \mathbb{D}=\omega_I(s)\dfrac{\partial}{\partial\boldsymbol{\varepsilon}}\dfrac{\partial(\psi_0-\psi_{0II})}{\partial\boldsymbol{\varepsilon}}+\omega_{II}(s)\dfrac{\partial}{\partial\boldsymbol{\varepsilon}}\dfrac{\partial\psi_{0II}}{\partial\boldsymbol{\varepsilon}}\end{cases}\end{cases} \tag{43}$$

where the value of β depends on the stress state: β=1 is used if $\bar{\sigma}^{\mathbf{nn}}>0$ and the failure

surface is an ellipse, otherwise $\beta=\bar{\beta}$ if $\bar{\sigma}^{\mathbf{nn}} \le 0$. For most materials, $\bar{\beta} \le 0$ since the failure compression strength f_c is much higher than the failure tension strength f_t, and the failure surface becomes a hyperbola. Thus, only the case $\bar{\beta} \le 0$ is considered and discussed.

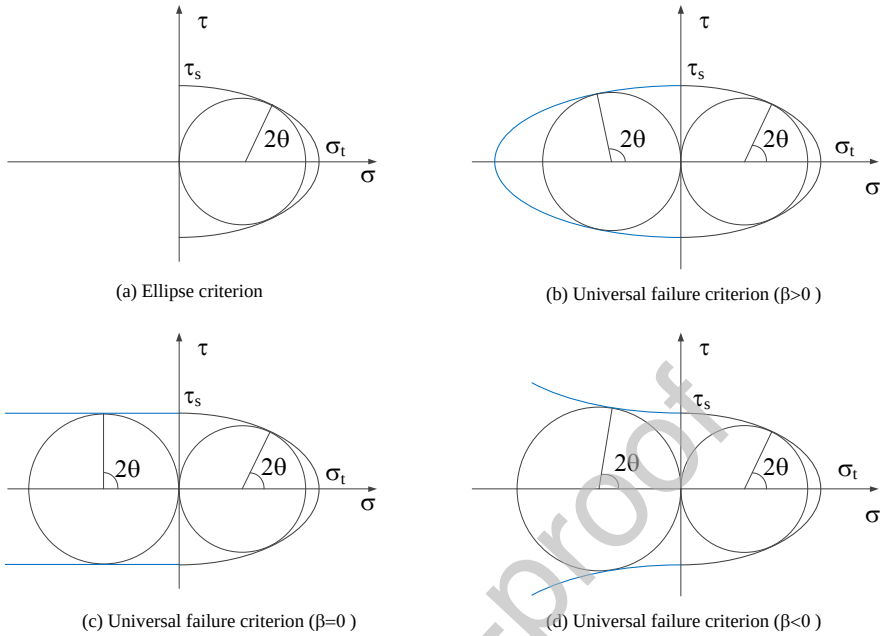

(a) Ellipse criterion (b) Universal failure criterion (β>0)

(c) Universal failure criterion (β=0) (d) Universal failure criterion (β<0)

Figure 2. The universal failure criterion.

3.3 The crack direction

The direction of the crack propagation can be determined based on the universal criterion, and one can define a new function as

$$f(2\theta)=\beta\frac{(\bar{\sigma}^{\mathbf{nn}})^2}{\sigma_t^2}+\frac{(\bar{\sigma}^{\mathbf{nm}})^2}{\tau_s^2}=\beta\frac{(r\cos 2\theta+a)^2}{\sigma_t^2}+\frac{(r\sin 2\theta)^2}{\tau_s^2} \tag{44}$$

where $r=(\bar{\sigma}_1-\bar{\sigma}_2)/2$, $a=(\bar{\sigma}_1+\bar{\sigma}_2)/2$, θ is the angle between the direction of $\bar{\sigma}^{\mathbf{nn}}$ and the direction of the first principal normal stress $\bar{\sigma}_1$, and $\mathbf{n}=[\cos(\theta+\theta_0),\sin(\theta+\theta_0)]$, in which θ_0 is the angle between the direction of the first principal normal stress $\bar{\sigma}_1$ and the direction of the x_1-axis. The crack direction $\mathbf{m}$ is perpendicular to the direction $\mathbf{n}$, which is the direction of stress $\bar{\sigma}^{\mathbf{nn}}$. According to the universal criterion, θ can be obtained as

$$\theta=\arg\max_{\theta\in[0,\pi/4]} f(2\theta) \tag{45}$$

and the derivative of f with respect to 2θ is

$$f'=\frac{\mathrm{d}f}{\mathrm{d}(2\theta)}=2r\sin 2\theta\frac{1}{\chi^2\sigma_t^2}[r(1-\beta\chi^2)\cos 2\theta-\beta\chi^2 a] \tag{46}$$

Then the value of θ can be evaluated for different cases:

(i) $\bar{\sigma}_1+\bar{\sigma}_2\geq 0$ and $\chi^2\leq(\bar{\sigma}_1-\bar{\sigma}_2)/(2\bar{\sigma}_1)$ (see Figure 3(a))

In this case, β=1 , $f'>0$ if $\cos 2\theta>\frac{a}{r}\frac{\chi^2}{(1-\chi^2)}$ and $f'<0$ if $\cos 2\theta<\frac{a}{r}\frac{\chi^2}{(1-\chi^2)}$. Thus

$$\theta=\frac{1}{2}\arccos\frac{\bar{\sigma}_1+\bar{\sigma}_2}{\bar{\sigma}_1-\bar{\sigma}_2}\frac{\chi^2}{(1-\chi^2)} \tag{47}$$

(ii) $\bar{\sigma}_1+\bar{\sigma}_2\geq 0$ and $(\bar{\sigma}_1-\bar{\sigma}_2)/(2\bar{\sigma}_1)\leq\chi^2$ (see Figure 3 (b))

In this case, β=1, and $f'<0$, thus θ=0.

(iii) $\bar{\sigma}_1+\bar{\sigma}_2<0$, $\bar{\sigma}_1>0$ and $\chi^2<(\bar{\sigma}_1-\bar{\sigma}_2)/(2\bar{\sigma}_1)$ (see Figure 3 (c))

For the case $\bar{\sigma}^{\mathbf{nn}}>0$, one has $f'<0$. For the case $\bar{\sigma}^{\mathbf{nn}}<0$ and $\beta\leq 0$, $f'>0$ if $\cos 2\theta>\frac{a\beta\chi^2}{r(1-\beta\chi^2)}$ and $f'<0$ if $\cos 2\theta<\frac{a\beta\chi^2}{r(1-\beta\chi^2)}$. Thus,

$$\theta=\frac{1}{2}\arccos\frac{\bar{\sigma}_1+\bar{\sigma}_2}{\bar{\sigma}_1-\bar{\sigma}_2}\frac{\beta\chi^2}{(1-\beta\chi^2)} \tag{48}$$

(iv) $\bar{\sigma}_1+\bar{\sigma}_2<0$, $\bar{\sigma}_1>0$ and $\chi^2\geq(\bar{\sigma}_1-\bar{\sigma}_2)/(2\bar{\sigma}_1)$ (see Figure 3 (d))

For the case $\bar{\sigma}^{\mathbf{nn}}>0$, $f'>0$ if $\cos 2\theta<\frac{a}{r}\frac{\chi^2}{(1-\chi^2)}$, and $f'<0$ if $\cos 2\theta>\frac{a}{r}\frac{\chi^2}{(1-\chi^2)}$. For the case $\bar{\sigma}^{\mathbf{nn}}<0$ and $\beta\leq 0$, $f'>0$ if $\cos 2\theta>\frac{a\beta\chi^2}{r(1-\beta\chi^2)}$ and $f'<0$ if $\cos 2\theta<\frac{a\beta\chi^2}{r(1-\beta\chi^2)}$. Thus

$$\theta=0 \quad or \quad \theta=\frac{1}{2}\arccos\frac{\bar{\sigma}_1+\bar{\sigma}_2}{\bar{\sigma}_1-\bar{\sigma}_2}\frac{\beta\chi^2}{(1-\beta\chi^2)} \tag{49}$$

(v) $\bar{\sigma}_1<0$ (see Figure 3 (c))

In this case, $\beta\leq 0$, $f'>0$ if $\cos 2\theta>\frac{a\beta\chi^2}{r(1-\beta\chi^2)}$ and $f'<0$ if

$\cos 2\theta < \dfrac{a\beta\chi^2}{r(1-\beta\chi^2)}$. Thus, θ can be computed by Equation (48).

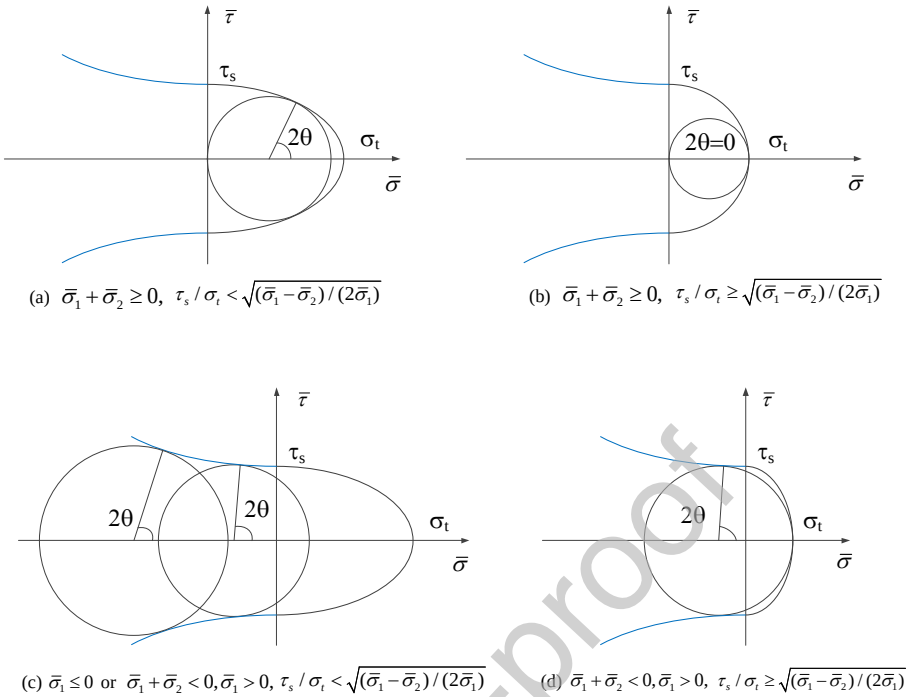

Figure 3 . The crack direction based on the universal failure criterion

4. Analytical solutions for a 2D bar under uniaxial tension and compression

In Equation (43), some unknown parameters need to be determined, such as $\bar{\beta}$ and coefficients a_i in the function $\omega(s)$ for a given softening law. To obtain these parameters, a 2D bar under uniaxial tension and compression shown in Figure 4 is analyzed. The solution of the universal failure criterion shown in Equation (38) is first introduced since the proposed phase-field model is based on this criterion.

4.1 Solution of the universal failure criterion

The details of the universal failure criterion can be found in [58] and only some relevant results are given here. The failure tension strength f_t and the critical tensional failure stress σ_t have the following relationship

$$f_t = \bar{k}_1 \sigma_t \tag{50}$$

with

$$\bar{k}_1 = \begin{cases} 2\chi\sqrt{1-\chi^2}, & if \quad \chi < \sqrt{1/2} \\ 1 & otherwise \end{cases} \tag{51}$$

Similarly, the relationship between the failure compressive strength f_c and the critical

tensional failure stress σ_t is

$$f_c = \bar{k}_2 \sigma_t \tag{52}$$

with

$$\bar{k}_2 = 2\chi\sqrt{1-\bar{\beta}\chi^2} \qquad for \quad \bar{\beta} \le 0 \tag{53}$$

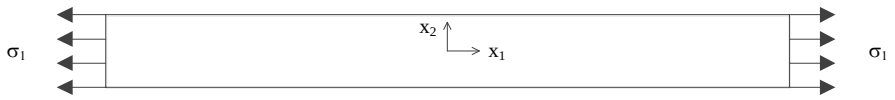

(a) Long bar under uniform tension

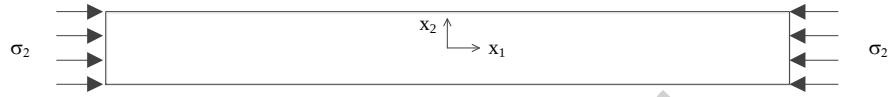

(b) Long bar under uniform compression

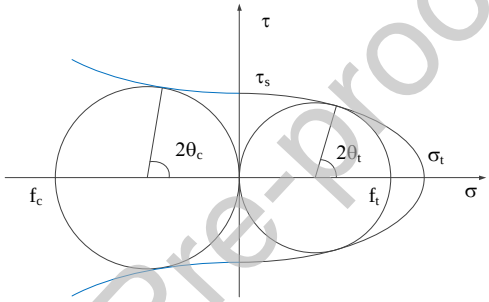

(c) Stress state for tension and compression

Figure 4. A 2D long bar under uniaxial tension and compression

The ratio f_c / f_t is much larger than 1.0 since $\bar{\beta} < 0$ for most materials, and it can explain why there is often an asymmetry between tensile and compressive strength for many materials.

Once f_t, f_c and χ are known, σ_t, τ_s, $\bar{\beta}$ can be obtained by

$$\sigma_t = f_t / \bar{k}_1, \qquad \tau_s = \chi\sigma_t \tag{54}$$

$$\bar{\beta} = \frac{1}{\chi^2} - \frac{f_c^2}{4\chi^2\tau_s^2} \tag{55}$$

The angle θ (θ_t or θ_c) shown in Figure 4 (c) can be computed by

$$\cos 2\theta = \frac{\sigma_1 - \sigma_2}{\sigma_1 + \sigma_2}\frac{\beta\chi^2}{1-\beta\chi^2} \tag{56}$$

where $\sigma_1 = \sigma > 0, \sigma_2 = 0$ and, $\beta = 1$ for uniform tension, and $\sigma_2 = -\sigma < 0, \sigma_1 = 0$ and, $\beta = \bar{\beta} \le 0$ for uniform compression. For uniform tension, the tensional-shear case is assumed, i.e., $\chi = \tau_s / \sigma_t < \sqrt{(\sigma_1 - \sigma_2)/(2\sigma_1)} = \sqrt{1/2}$.

4.2 Solution of the phase-field model

Now consider a 2D bar under uniform compression (Figure 4(b)). Substituting Equation (56) into Equation (42), one has

$$\frac{1}{4}\beta\frac{(\sigma\cos 2\theta-\sigma)^2}{\sigma_t^2}+\frac{1}{4}\frac{\sigma^2\sin^2 2\theta}{\tau_s^2}=-\frac{2l_0^2\nabla^2 s-\alpha'(s)}{\alpha'(0)}\frac{\phi'(0)}{\phi'(s)} \tag{57}$$

where the equality of the evolution equation is used and it can be further simplified to

$$\frac{\sigma^2}{\sigma_t^2}\frac{1}{k_2^2}=-\frac{2l_0^2\nabla^2 s-\alpha'(s)}{\alpha'(0)}\frac{\phi'(0)}{\phi'(s)} \tag{58}$$

where $k_2=2\chi\sqrt{1-\beta\chi^2}=\bar{k}_2$.

Substituting σ_t in Equation (43) into Equation (58), one can obtain

$$2l_0^2\nabla^2 s-\alpha'(s)+\frac{\sigma^2}{2E\bar{G}_{cI}}\frac{c_0 l_0}{k_2^2}\phi'(s)=0 \tag{59}$$

or, equivalently,

$$(l_0\nabla s)^2-\alpha(s)+\frac{\sigma^2}{2E\bar{G}_{cI}}\frac{c_0 l_0}{k_2^2}\phi(s)=0 \tag{60}$$

Assuming that the crack initiation is at the middle point of the long bar, the stress σ can be computed by

$$\sigma(s^*)=\sqrt{\frac{2k_2^2E\bar{G}_{cI}}{c_0 l_0}\frac{\alpha(s^*)}{\phi(s^*)}} \tag{61}$$

where $\nabla s=0$ at the middle point is assumed and s^* is the maximum value of s. Then the failure compression strength can be determined upon the instant of damage initiation by

$$f_c=\lim_{s^*\to 0}\sigma(s^*)=\sqrt{\frac{2k_2^2E\bar{G}_{cI}}{c_0 l_0}\frac{\alpha'(0)}{\phi'(0)}}=k_2\sigma_t=\bar{k}_2\sigma_t \tag{62}$$

which is the same as Equation (52).

Similarly, for the bar under tensional loading, the stress σ can be computed by

$$\sigma(s^*)=\sqrt{\frac{2k_1^2E\bar{G}_{cI}}{c_0 l_0}\frac{\alpha(s^*)}{\phi(s^*)}} \tag{63}$$

where $k_1=\bar{k}_1$, and the failure tension strength f_t (see Figure 4(c)) can be computed by

$$f_t=\lim_{s^*\to 0}\sigma(s^*)=\sqrt{\frac{2k_1^2E\bar{G}_{cI}}{c_0 l_0}\frac{\alpha'(0)}{\phi'(0)}}=k_1\sigma_t=\bar{k}_1\sigma_t \tag{64}$$

which is the same as Equation (50).

If using Equation (12) and Equation (17) for functions $\alpha(s)$ and $\phi(s)$, one can compute a_1 in Equation (17) as

$$a_1 = \frac{2\xi k_1^2}{c_0 l_0}\frac{E\bar{G}_{cI}}{f_t^2} = \frac{2\xi}{c_0 l_0}\frac{EG_c^t}{f_t^2} \tag{65}$$

where

$$G_c^t = \bar{G}_{cI} k_1^2 \tag{66}$$

Equations (65) and (66) can also be obtained from Equation (62), which means if the same length scale l_0 is used for tensional-shear and compressive-shear fractures, the same a_1 will be obtained, i.e., there is no need to use different l_0 for different fracture patterns. Note that E should be replaced by $E/(1-\nu^2)$ for plane strain problems, where ν is the Poisson's ratio.

General softening laws can also be implemented in the proposed model and the solution can be found in [59]. The derivation is similar and only the main results are given here. The other parameters in Equation (17) can be obtained by different softening laws as

$$a_2 = \frac{1}{\xi}[(-\frac{4\pi\xi^2}{c_0}\frac{G_c^t}{f_t^2}k_0)^{\frac{2}{3}}+1]-(p+1) \tag{67}$$

$$a_2 a_3 + a_2 a_3 a_4 + \cdots = \begin{cases} 0, & p > 2 \\ \frac{1}{\xi}(\frac{c_0 w_c f_t}{2\pi G_c^t})^2 - (1+a_2), & p = 2 \end{cases} \tag{68}$$

where k_0 and w_c are the initial slope and the ultimate crake opening, respectively. In this paper, $\xi = 2$ is used and the linear softening law is considered with

$$a_2 = -\frac{1}{2}, \quad a_i = 0, \quad i \geq 3 \tag{69}$$

It should be noted that other phase-field models with a value $\xi \in [0,2)$ can also be implemented in the proposed model, such as the phase-field model with $\xi = 0$ for cohesive fracture [66].

In this paper, the same softening law is used for both tensile and compressive loadings. Thus, all the parameters a_i in the compressive-shear fracture are the same as those in the tensional-shear fracture.

5. Implementation

The proposed model can be implemented with the finite element method (FEM). A staggered

algorithm is applied to solve the equilibrium equation and the evolution equation separately as two sub-problems in each iteration or load step. The whole simulation will be discretized into M load steps based on the direct displacement control. In the load step $m+1$, the equilibrium equation and the evolution equation are solved with the assumption that all the variables in the load step m are known.

The evolution equation (43) is an evolution inequality and the boundedness condition for phase-field cannot be guaranteed. It can be considered a bound-constrained complementarity problem [69] and some efficient methods can be applied to solve this problem, such as the reduced-space active set Newton method [70], or one can use the solver included in the open-source toolkit PETSc [69].

The inequality in the evolution equation holds when $s=0$ and $\delta s=0$, i.e., the material is not damaged; on the contrary, the equality holds when the material is damaged ($s>0$). Thus, the inequality becomes a quality when $s\to 0$ and the evolution equation can be written as

$$\omega_I'(0)\beta\frac{\psi_{0I}}{G_{cI}}+\omega_{II}'(0)\frac{\psi_{0II}}{G_{cII}}=-\frac{\alpha'(0)}{c_0 l_0} \tag{70}$$

where $\nabla^2 s=0$ is assumed when $s=0$. Equation (70) can be rewritten as

$$\frac{\beta\psi_{0I}}{\bar{G}_{cI}}+\frac{\psi_{0II}}{\bar{G}_{cII}}=\frac{\alpha'(0)}{c_0 l_0\phi'(0)}=F_{\min} \tag{71}$$

and the evolution equation can be changed to

$$\frac{\omega_I'(s)}{b_I}F_I+\frac{\omega_{II}'(s)}{b_{II}}F_{II}=\frac{2l_0}{c_0}\nabla^2 s-\frac{\alpha'(s)}{c_0 l_0} \tag{72}$$

where $F_I+F_{II}=\max[\beta\frac{\psi_{0I}}{\bar{G}_{cI}}+\frac{\psi_{0II}}{\bar{G}_{cII}},F_{\min}]$. Also note that $F_{\min}=0$ for the classical phase-field model.

To handle the irreversibility [47] in general scenarios, one can introduce the non-decreased history field $\hbar=\hbar_I+\hbar_{II}$ as

$$\begin{cases}\hbar_I(m)=\beta\dfrac{\psi_{0I}(m)}{\bar{G}_{cI}},\hbar_{II}=\dfrac{\psi_{0II}(m)}{\bar{G}_{cII}}, & if\quad \beta\dfrac{\psi_{0I}(m)}{\bar{G}_{cI}}+\dfrac{\psi_{0II}(m)}{\bar{G}_{cII}}>\hbar_I(m-1)+\hbar_{II}(m-1)\\ \hbar_I(m)=\hbar_I(m-1),\hbar_{II}=\hbar_{II}(m-1), & if\quad \beta\dfrac{\psi_{0I}(m)}{\bar{G}_{cI}}+\dfrac{\psi_{0II}(m)}{\bar{G}_{cII}}\le\hbar_I(m-1)+\hbar_{II}(m-1)\end{cases} \tag{73}$$

where $\hbar_I(m)$ and $\hbar_{II}(m)$ are history fields at load step m, and

$\hbar_I(0)+\hbar_{II}(0)=\max[\beta\frac{\psi_{0I}(0)}{\bar{G}_{cI}}+\frac{\psi_{0II}(0)}{\bar{G}_{cII}},F_{\min}]$ at the initial step 0.

Finally, the main formulations for the proposed phase-field model are

$$\begin{cases}\begin{cases}\dfrac{\omega_I'(s)}{b_I}\hbar_I+\dfrac{\omega_{II}'(s)}{b_{II}}\hbar_{II}=\dfrac{2l_0}{c_0}\nabla^2 s-\dfrac{\alpha'(s)}{c_0 l_0}\\ \psi_{0I}=\dfrac{1}{2E}(\bar{\sigma}^{\mathbf{nn}})^2,\psi_{0II}=\dfrac{1}{2\mu}(\bar{\sigma}^{\mathbf{nm}})^2\end{cases}\\ \bar{G}_{cI}=G_c^t/k_1^2,\bar{G}_{cII}=\chi^2\dfrac{\bar{G}_{cI}E}{\mu}\\ \sigma_t=f_t/k_1,\tau_s=\chi\sigma_t,\bar{\beta}=1/\chi^2-f_c^2/(4\chi^2\tau_s^2)\end{cases}\\ \begin{cases}\mathrm{div}\boldsymbol{\sigma}=\mathbf{0}\\ \boldsymbol{\sigma}=\omega_I(s)\dfrac{\partial(\psi_0-\psi_{0II})}{\partial\boldsymbol{\varepsilon}}+\omega_{II}(s)\dfrac{\partial\psi_{0II}}{\partial\boldsymbol{\varepsilon}}\\ \mathbb{D}=\omega_I(s)\dfrac{\partial}{\partial\boldsymbol{\varepsilon}}\dfrac{\partial(\psi_0-\psi_{0II})}{\partial\boldsymbol{\varepsilon}}+\omega_{II}(s)\dfrac{\partial}{\partial\boldsymbol{\varepsilon}}\dfrac{\partial\psi_{0II}}{\partial\boldsymbol{\varepsilon}}\end{cases}\end{cases}\tag{74}$$

Table 1. The material parameters used in different phase-field models

Phase-field model	Input material parameters
Classical phase-field model [48]	(1) Elasticity modulus;(2) Poisson's ratio; (3) Fracture toughness.
Unified phase-field theory [59]	(1) Elasticity modulus; (2) Poisson's ratio; (3) Fracture toughness; (4) Failure tension strength.
Modified phase-field model [52]	(1) Elasticity modulus; (2) Poisson's ratio; (3) Mode-I fracture toughness; (4) Mode-II fracture toughness.
Mixed-mode phase-field model [54, 67]	(1) Elasticity modulus; (2) Poisson's ratio; (3) Mode-I fracture toughness; (4) Mode-II fracture toughness.
Phase-field model for compressive shear fractures [57]	(1) Elasticity modulus; (2) Poisson's ratio; (3) Fracture toughness; (4) Cohesion; (5) Internal friction angle.
Phase-field model for compressive shear fractures [56]	(1) Elasticity modulus; (2) Poisson's ratio; (3) Fracture toughness; (4) Cohesion; (5) Internal friction angle.
Mixed-mode phase-field model for tensional-shear fracture [55]	(1) Elasticity modulus; (2) Poisson's ratio; (3) Fracture toughness; (4) Failure tension strength; (5) Ratio of critical shear failure stress to critical normal fracture stress.
Proposed phase-field model for tensional-shear and compressive shear fractures	(1) Elasticity modulus; (2) Poisson's ratio; (3) Fracture toughness; (4) Failure tension strength; (5) Failure compression strength; (6) Ratio of critical shear failure stress to critical normal

	fracture stress.

The material parameters needed are: the elasticity modulus E, the Poisson's ratio ν, the fracture toughnesses G_c^t, the failure tension strength f_t, the failure compression strength f_c, and the ratio $\chi = \tau_s / \sigma_t$. Compared with the classical phase-field model, three additional parameters are needed and a list of the material parameters used in different models is shown in Table 1.

Remark 5.1. Equation (74) shows that the parameters $\bar{G}_{cI}$, $\bar{G}_{cII}$, k_1 and $\bar{\beta}$ are independent of the given softening law. Thus, the classical brittle phase-field model with $\alpha(s) = s^2$ and $\omega(s) = (1-s)^2$, and the phase-field model proposed in [66] coupled with general softening laws can also be incorporated into the proposed model.

The material parameters needed in the proposed modes can be obtained by two experiments: the tension experiment and the compression experiment, which can obtain the tension strength f_t, the failure compression strength f_c, and the corresponding failure angles θ_t and θ_c (see Figure 4(b)). More details for obtaining these parameters can be found in [58]. After these parameters are obtained, if the fracture toughness G_c^t is measured from the tension experiment, then G_{cI} and G_{cII} can be obtained, i.e. only one fracture toughness is needed.

The Galerkin weak form for the equilibrium equation and evolution equation can be written as

$$\int_\Omega \boldsymbol{\sigma} : \delta\boldsymbol{\varepsilon} \mathrm{d}\Omega = \int_{\partial\Omega} \bar{\mathbf{t}} \cdot \delta\mathbf{u} \mathrm{d}\partial\Omega \tag{75}$$

$$\int_\Omega \frac{2l_0}{c_0} \nabla s \cdot \delta(\nabla s) \mathrm{d}\Omega + \int_\Omega \frac{\alpha'(s)}{c_0 l_0} \delta s \mathrm{d}\Omega + \int_\Omega [\frac{\omega_I'(s)}{b_I} \hbar_I + \frac{\omega_{II}'(s)}{b_{II}} \hbar_{II}] \delta s \mathrm{d}\Omega = 0 \tag{76}$$

where the boundary conditions (4) and (5) are applied. FEM is used to discretize the above equations in this paper. The displacement $\mathbf{u}$, strain $\boldsymbol{\varepsilon}$ and phase-field s can be approximated as

$$\mathbf{u}(\mathbf{x}) = \boldsymbol{\Phi}_u(\mathbf{x})\hat{\mathbf{u}}, \quad \boldsymbol{\varepsilon}(\mathbf{x}) = \mathbf{B}_u(\mathbf{x})\hat{\mathbf{u}}, \quad s(\mathbf{x}) = \boldsymbol{\Phi}_s(\mathbf{x})\hat{\mathbf{s}}, \quad \nabla s(\mathbf{x}) = \mathbf{B}_s(\mathbf{x})\hat{\mathbf{s}} \tag{77}$$

where $\hat{\mathbf{u}}$ and $\hat{\mathbf{s}}$ are the nodal displacement and phase-field vectores, and in 2D case

$$\boldsymbol{\Phi}_u(\mathbf{x}) = \begin{bmatrix} \Phi^1 & 0 & \Phi^2 & 0 & \cdots & \Phi^N & 0 \\ 0 & \Phi^1 & 0 & \Phi^2 & \cdots & 0 & \Phi^N \end{bmatrix} \tag{78}$$

$$\mathbf{B}_u(\mathbf{x})=\begin{bmatrix} \Phi^1_{,1} & 0 & \Phi^2_{,1} & 0 & \cdots & \Phi^N_{,1} & 0 \\ 0 & \Phi^1_{,2} & 0 & \Phi^2_{,2} & \cdots & 0 & \Phi^N_{,2} \\ \Phi^1_{,2} & \Phi^1_{,1} & \Phi^2_{,2} & \Phi^2_{,1} & \cdots & \Phi^N_{,2} & \Phi^N_{,1} \end{bmatrix} \tag{79}$$

$$\mathbf{\Phi}_s(\mathbf{x})=\begin{bmatrix} \Phi^1 & \Phi^2 & \cdots & \Phi^N \end{bmatrix} \tag{80}$$

$$\mathbf{B}_s(\mathbf{x})=\begin{bmatrix} \Phi^1_{,1} & \Phi^2_{,1} & \cdots & \Phi^N_{,1} \\ \Phi^1_{,2} & \Phi^2_{,2} & \cdots & \Phi^N_{,2} \end{bmatrix} \tag{81}$$

where $\Phi^j=\Phi^j(\mathbf{x})$ are the shape functions and N is the number of total discrete nodes.

Substituting Equation (77) into Equations (75) and (76), one can obtain

$$\int_\Omega \mathbf{D}\mathbf{B}_u\hat{\mathbf{u}}\delta(\mathbf{B}_u\hat{\mathbf{u}})\mathrm{d}\Omega=\int_{\partial\Omega}\bar{\mathbf{t}}\cdot\delta(\mathbf{\Phi}_u\hat{\mathbf{u}})\mathrm{d}\partial\Omega \tag{82}$$

$$\int_\Omega \frac{2l_0}{c_0}\mathbf{B}_s\hat{\mathbf{s}}\cdot\delta(\mathbf{B}_s\hat{\mathbf{s}})\mathrm{d}\Omega+\int_\Omega \frac{\alpha'(s)}{c_0l_0}\delta(\mathbf{\Phi}_s\hat{\mathbf{s}})\mathrm{d}\Omega+\int_\Omega [\frac{\omega_I'(s)}{b_I}\hbar_I+\frac{\omega_{II}'(s)}{b_{II}}\hbar_{II}]\delta(\mathbf{\Phi}_s\hat{\mathbf{s}})\mathrm{d}\Omega=0 \tag{83}$$

where $\mathbf{D}$ is the degraded elasticity matrix. Finally, Equations (82) and (83) can be rewritten as

$$\int_\Omega \mathbf{B}_u^{\mathrm{T}}\mathbf{D}\mathbf{B}_u\mathrm{d}\Omega\hat{\mathbf{u}}=\int_{\partial\Omega}\mathbf{\Phi}_u^{\mathrm{T}}\bar{\mathbf{t}}\mathrm{d}\partial\Omega \tag{84}$$

$$\int_\Omega \frac{2l_0}{c_0}\mathbf{B}_s^{\mathrm{T}}\mathbf{B}_s\mathrm{d}\Omega\hat{\mathbf{s}}+\int_\Omega \frac{1}{c_0l_0}\alpha'(s)\mathbf{\Phi}_s^{\mathrm{T}}\mathrm{d}\Omega+\int_\Omega [\frac{\omega_I'(s)\hbar_I}{b_I}+\frac{\omega_{II}'(s)\hbar_{II}}{b_{II}}]\mathbf{\Phi}_s^{\mathrm{T}}\mathrm{d}\Omega=0 \tag{85}$$

If $b_I=b_{II}$ is used, the proposed model can be considered a special model, and Equation (84) will result in a linear system of equations as

$$\mathbf{K}_u\hat{\mathbf{u}}=\mathbf{F}_u \tag{86}$$

which can be solved robustly with

$$\mathbf{K}_u=\int_\Omega \mathbf{B}_u^{\mathrm{T}}\mathbf{D}\mathbf{B}_u\mathrm{d}\Omega,\qquad \mathbf{F}_u=\int_{\partial\Omega}\mathbf{\Phi}_u^{\mathrm{T}}\mathbf{t}\mathrm{d}\partial\Omega \tag{87}$$

The non-linear system of equations obtained by Equation (85) can be solved by Newton's method. In each iteration step, a linearized system of equations can be obtained as

$$\mathbf{F}'(\hat{\mathbf{s}}^k)\Delta\hat{\mathbf{s}}^{k+1}=-\mathbf{F}(\hat{\mathbf{s}}^k) \tag{88}$$

with

$$\mathbf{F}'(\hat{\mathbf{s}}^k)=\int_\Omega \frac{2l_0}{c_0}\mathbf{B}_s\mathbf{B}_s^{\mathrm{T}}\mathrm{d}\Omega+\int_\Omega \frac{\alpha''(\mathbf{\Phi}_s\hat{\mathbf{s}}^k)}{c_0l_0}\mathbf{\Phi}_s^{\mathrm{T}}\mathbf{\Phi}_s\mathrm{d}\Omega+\int_\Omega [\frac{\omega_I''(\hat{\mathbf{s}}^k)\hbar_I}{b_I}+\frac{\omega_{II}''(\hat{\mathbf{s}}^k)\hbar_{II}}{b_{II}}]\mathbf{\Phi}_s^{\mathrm{T}}\mathbf{\Phi}_s\mathrm{d}\Omega \tag{89}$$

$$\mathbf{F}(\hat{\mathbf{s}}^k)=\int_\Omega \frac{2l_0}{c_0}\mathbf{B}_s\mathbf{B}_s^{\mathrm{T}}\mathrm{d}\Omega\hat{\mathbf{s}}^k+\int_\Omega \frac{\alpha'(\mathbf{\Phi}_s\hat{\mathbf{s}}^k)}{c_0l_0}\mathbf{\Phi}_s\mathrm{d}\Omega+\int_\Omega [\frac{\omega_I'(\hat{\mathbf{s}}^k)\hbar_I}{b_I}+\frac{\omega_{II}'(\hat{\mathbf{s}}^k)\hbar_{II}}{b_{II}}]\mathbf{\Phi}_s\mathrm{d}\Omega \tag{90}$$

where $\hat{\mathbf{s}}^k$ are the nodal phase-field at the iteration step k and $\Delta\hat{\mathbf{s}}^{k+1}=\hat{\mathbf{s}}^{k+1}-\hat{\mathbf{s}}^k$.

In this paper, the general case $b_I\neq b_{II}$ is also considered, and the following equation is used

to determine b_I and b_{II} at step *m*:

$$\begin{cases} b_I(m)=(\cos 2\theta)^{\kappa}, b_{II}=(\sin 2\theta)^{\kappa}, & if \quad \beta\dfrac{\psi_{0I}(m)}{\bar{G}_{cI}}+\dfrac{\psi_{0II}(m)}{\bar{G}_{cII}} > \hbar_I(m-1)+\hbar_{II}(m-1) \\ b_I(m)=b_I(m-1), b_{II}=b_{II}(m-1), & if \quad \beta\dfrac{\psi_{0I}(m)}{\bar{G}_{cI}}+\dfrac{\psi_{0II}(m)}{\bar{G}_{cII}} \le \hbar_I(m-1)+\hbar_{II}(m-1) \end{cases} \tag{91}$$

where κ is a given parameter. Equation (91) can be reduced to $b_I=1, b_{II}=0$ for pure tensional fracture and $b_I=0, b_{II}=1$ for pure shear fracture.

6. Results

In this section, some numerical examples are tested to verify the proposed model. In all the examples, the plane stress state and linear softening law in the unified phase-field theory [59] with $\alpha(s)=2s-s^2$ are assumed if not specified otherwise. The tensional-shear fracture has been investigated in previous work [55]. Thus, only the compressive-shear and tensional-compressive-shear fractures are tested in this paper.

The special model with $b_I=b_{II}=1.0$ will be used in the examples since it can obtain similar crack paths as the non-special model, which has been observed for tensional-shear fracture [55]. Several advantages can be achieved by using the special model. Firstly, there is no need to choose different functions of b_I and b_{II}. Secondly, the equilibrium equation will result in a linear system of equations, which is much easier to be solved and the problem converges much faster. Thirdly, it is much more suitable for simulating crack branching since there is no need to compute the crack angles while solving the equilibrium equation.

6.1 Single-inclined notched rock plate under uniaxial compression

A rock plate with a single-inclined notch at the center under uniaxial compression shown in Figure 5(a) is tested in this example and the length of the plate is 20.32mm. Many researchers have investigated the cracking behavior in specimens under compression [71-74] and two typical fracture patterns are shown in Figure 5. The fracture behavior shown in Figure 5(b) was reported in [73], in which the tensile cracks initiate first and then the normal shear cracks appear. The fracture behavior shown in Figure 5(c) was reported in [71, 75], in which wing cracks emerge first, and secondary cracks appear and propagate until rupture. It will be shown in this example that these two fracture behaviors can be obtained by the proposed model.

The material properties used are [71]: Young's modulus $E=36.2$ GPa, Poisson's ratio $\nu=0.21$, the failure tension strength $f_t=10.25$ MPa. Triangular elements are used to discretize the domain with fine meshes (the mesh size is about 0.1mm) assigned to the critical zones and the

two length scales l_0=0.25 and 0.5mm are used. Two models, i.e., the linear softening model and the classical brittle model, are implemented in the proposed phase-field model. In the linear softening model, $\alpha(s)=2-2s^2$ and $\omega(s)=1/[1+\phi(s)]$ with linear softening law is used, while $\alpha(s)=s^2$ and $\omega(s)=(1-s)^2$ is used in the classical brittle model.

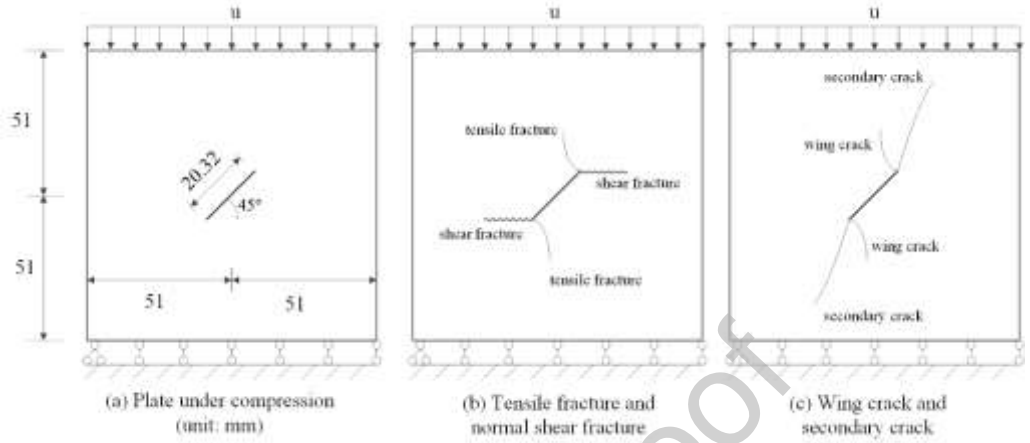

Figure 5. Crack behavior observed in some experiments: (a) model and boundary conditions (b) tensile fracture and normal shear fracture [73]; (c) wing crack and secondary crack [71].

In order to show the advantages of the proposed phase-field model, three sets of material properties are used to observe the different crack patterns.

6.1.1 Compressive-shear fracture

In this test, the fracture toughness $G_c^t=11$N/mm and $\chi=0.6$ are taken. In the first simulation, the failure compression strength f_c=12.8125 MPa is chosen to ensure $\bar{\beta}=0$. The sensitivity of the results to the displacement increment is studied and the results are shown in Figure 6(a). It can be observed that the peak force decreases as the displacement increment decreases, and the peak force will converge to a fixed value. According to Figure 6(a), the displacement increment Δu =0.5×10^{-4} mm is applied in the following tests in this simulation.

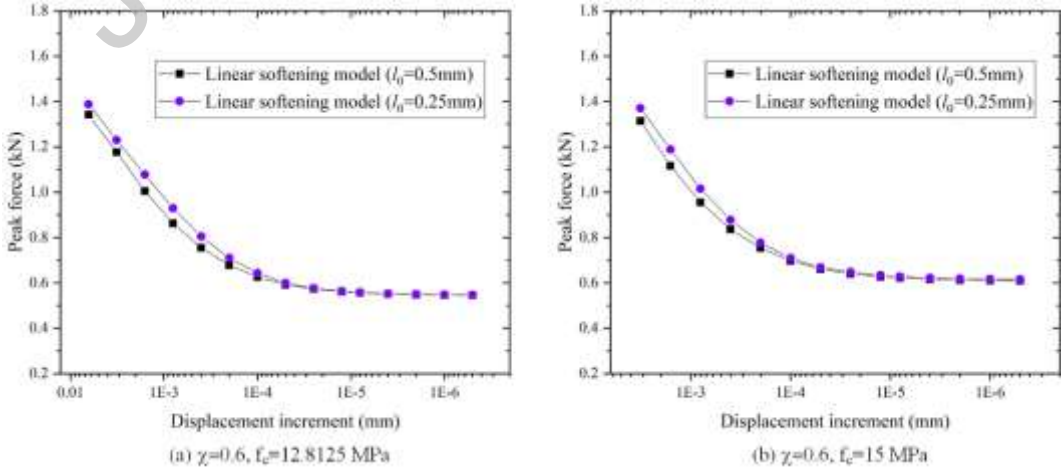

Figure 6. Sensitivity of the results to the displacement increment

The crack paths obtained by the linear softening model and the classical brittle model with different length scales are shown in Figure 7 and Figure 8, respectively. One can observe that only shear fractures are obtained.

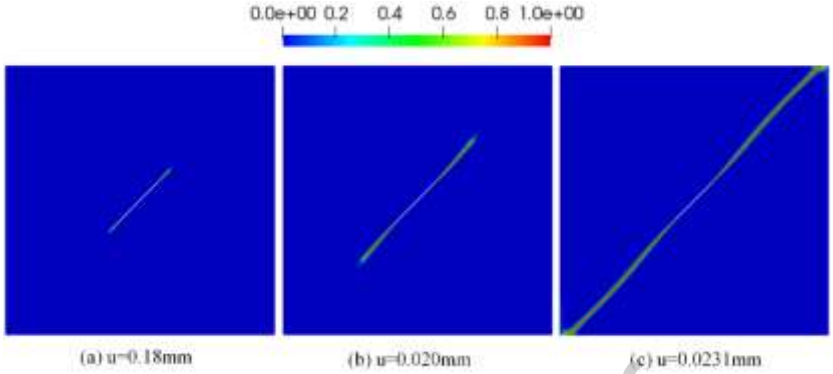

Figure 7. Crack path for single-inclined notched plate under compression (linear softening model, χ=0.6, f_c=12.8125 MPa, l_0 = 0.25mm)

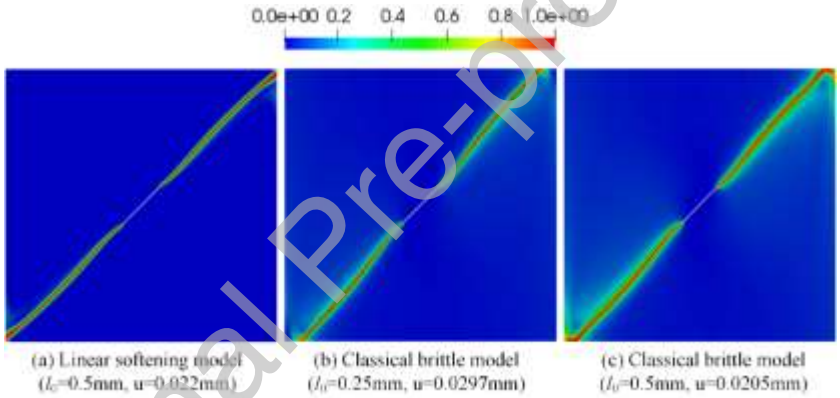

Figure 8. Crack paths for single-inclined notched plates under compression (χ=0.6, f_c=12.8125 MPa)

In the second simulation, the failure compression strength f_c =15 MPa is used which gives $\bar{\beta}$ =-1.0295. The sensitivity of the results to the displacement increment is also studied in this simulation and the results are shown in Figure 6(b). The results are similar to those obtained in the first simulation and the displacement increment Δu =0.5×10^{-4} mm is applied in the following tests in this simulation.

The crack paths obtained by the proposed phase-field model are shown in Figure 9 and Figure 10. Similar to the first simulation, only the compressive-shear fractures are observed and the both linear softening model and the classical brittle model obtain similar crack paths. Compared with the crack paths obtained in the previous simulation ($\bar{\beta}=0$), the crack paths in this simulation are extended to the top and bottom boundaries. The load-displacement curves for these two simulations are shown in Figure 11. It can be observed that the influence of the length

scale in the linear softening model is much less than in the classical brittle model.

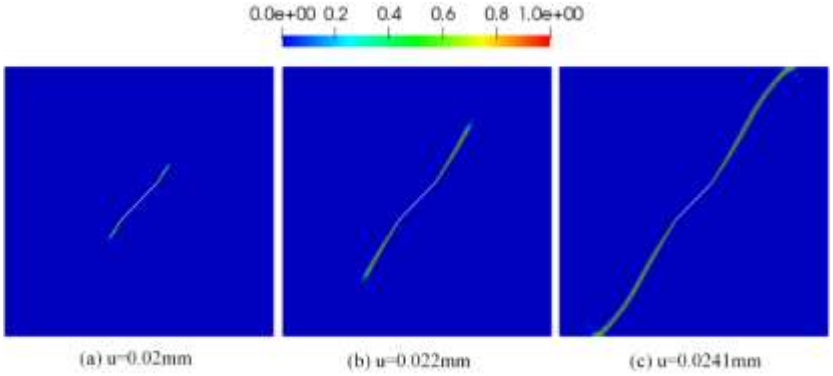

Figure 9. Crack path for single-inclined notched plate under compression (linear softening model, χ=0.6, f_c=15 MPa, l_0 = 0.25mm)

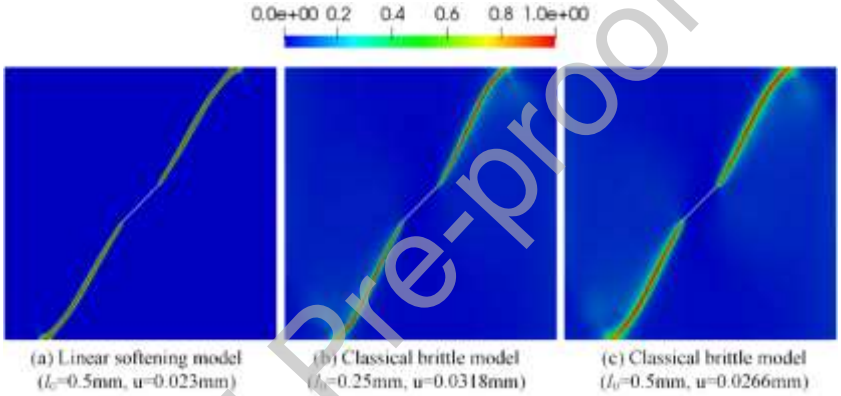

Figure 10. Crack paths for single-inclined notched plates under compression (χ=0.6, f_c=15 MPa)

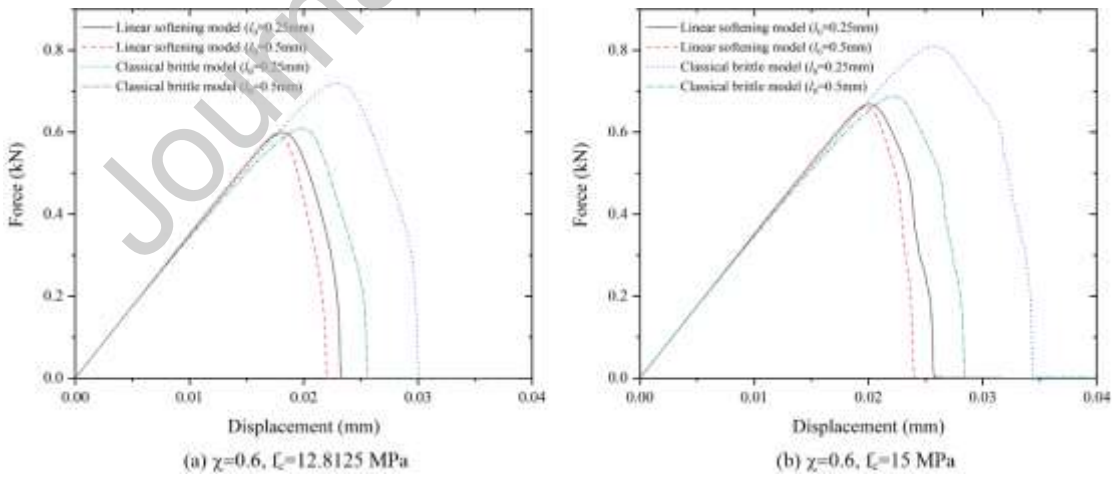

Figure 11. Load-displacement curves for the single-inclined notched plate under compression (χ=0.6)

6.1.2 Tensile and normal shear fractures

In this test, the fracture toughness $G_c^t = 5$ N/mm, $\chi = 2.0$ and $f_c = 41$ MPa are used, and $\bar{\beta} = 0$ is achieved. The displacement increment Δu is 0.5×10^{-4} mm in all the tests. The

crack paths are shown in Figure 12 and Figure 13. Two tensile cracks emerge first and are followed by two normal shear cracks, which agree with the experimental results [73]. The load-displacement curves are shown in Figure 16(a), and it can be observed that the length scale influences the global response of the structure in both the linear softening model and the classical brittle model. However, the influence in the linear softening model is much less than that in the classical brittle model.

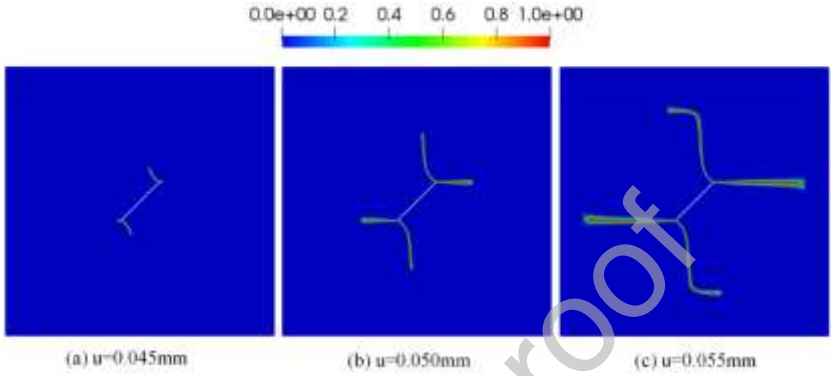

Figure 12. Crack path for the single-inclined notched plate under compression (linear softening model, χ=2.0, f_c=41MPa, l_0 = 0.25mm)

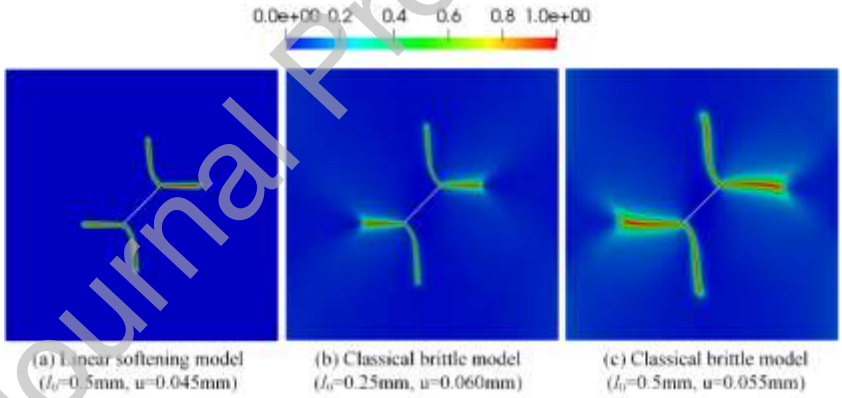

Figure 13. Crack paths for the single-inclined notched plates under compression (χ=2.0, f_c=41MPa)

6.1.3 Tensile and inclined shear fractures

In this test, the fracture toughness G_c^t =11N/mm, $\chi = 2.0$ and the failure compression strength f_c=65 MPa are used and $\overline{\beta}$ =-0.3783 is achieved. The displacement increment Δu is 0.5×10^{-4} mm in all the tests. The crack paths obtained by the proposed model with the linear softening model and the classical brittle model are shown in Figure 14 and Figure 15. Two wing cracks and two secondary cracks are observed in all the examples, which agree with the experimental results [71]. The load-displacement curves are shown in Figure 16(b). It can also be

observed that the influence of the length scale in the linear softening model is much less than that in the classical brittle model.

The mesh size h used in this example is about $(2/5 \sim 1/5)\ l_0$ in all the tests, and the results may not be accurate since the mesh size h is not sufficiently small compared to the length scale l_0. To obtain more accurate results, $h = (1/10 \sim 1/5)\ l_0$ is suggested in the unified phase-field theory [59, 76].

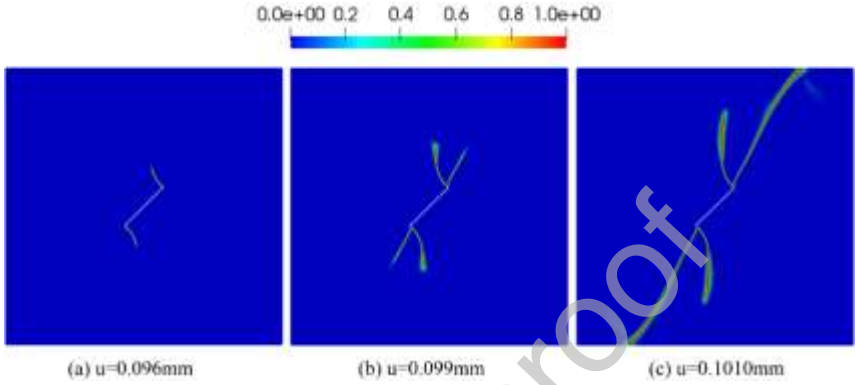

Figure 14. Crack path for the single-inclined notched plate under compression (linear softening model, χ=2.0, f_c =82MPa, l_0=0.25mm)

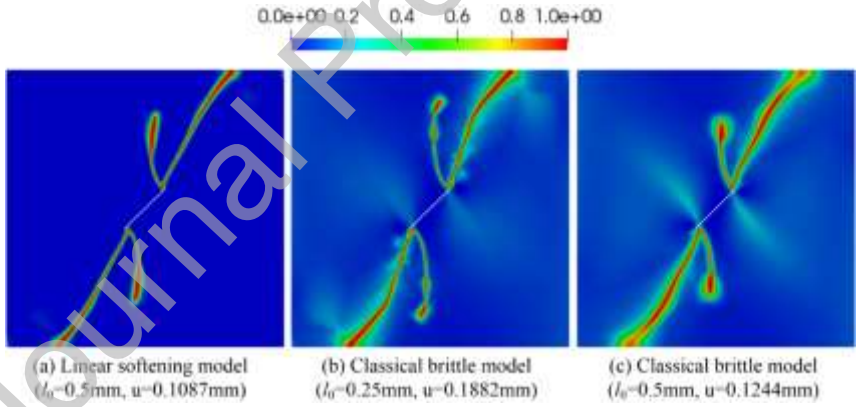

Figure 15. Crack paths for the single-inclined notched plates under compression (linear softening model, χ=2.0)

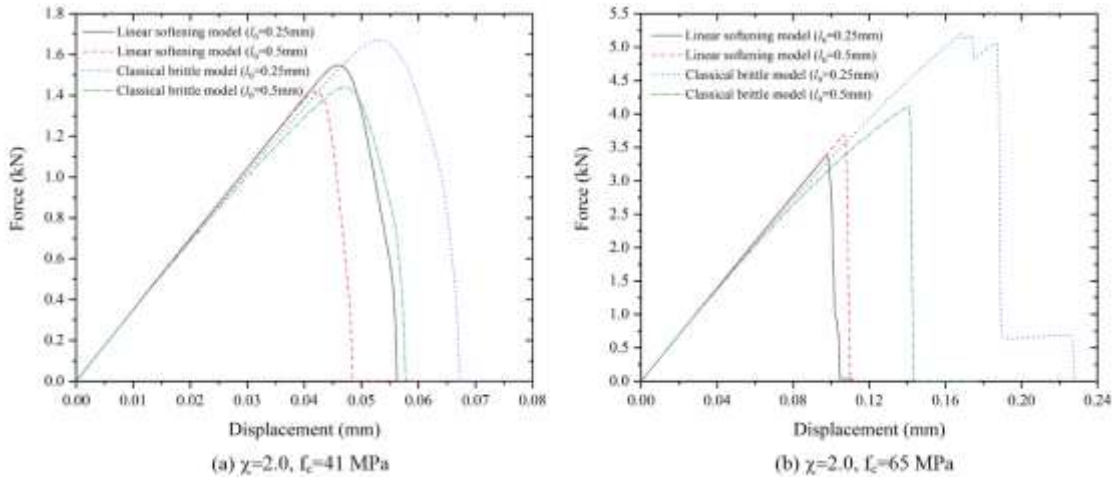

Figure 16. Load-displacement curves for the single-inclined notched plate under compression (χ=2.0)

6.2 Rock plates with two inclined notches under uniaxial compression

In this example, three rock plates with double notches under compression shown in Figure 17 are tested. The height and width of the three specimens are all 152.4mm and 76.2mm, respectively. The length of each notch is 2a=12.7mm, and the angle of the notch is ϑ. In this example, the notation "$\vartheta-w-c$" is used to represent the geometry of the notches of each specimen (see Figure 17). For example, "45-0-2a" means that the angle of the notch is $\vartheta=45°$, the spacing $w=0$, the continuity $c=2a$. The crack paths observed in the experiment tests [77-79] for three cases "45-0-2a", "45-a-2a" and "45-2a-2a" are summarized in Figure 18.

In our simulation, these three specimens are considered and the material properties used are [52]: Young's modulus $E=5.96$ GPa, Poisson's ratio $v=0.24$, fracture toughness $G_c^t=5.0$ N/m and the failure tension strength $f_t=2.3$ MPa. For each specimen, four sets of χ and failure compression strength are tested: (i) χ=0.6, $f_c=2.875$ MPa ($\bar{\beta}$ =0); (ii) χ=0.6, $f_c=3.594$ MPa ($\bar{\beta}=-1.5625$); (ii) χ=3.0, $f_c=13.8$ MPa ($\bar{\beta}=0$); and (iv) χ=3.0, $f_c=16.1$ MPa ($\bar{\beta}=-0.0412$). The displacement increment Δu is 10^{-4} mm. Both the linear softening model and the classical brittle model are used to compare the results. The mesh size is about 0.1mm in the critical zones and two length scales l_0 =0.3 and 0.6 mm are tested.

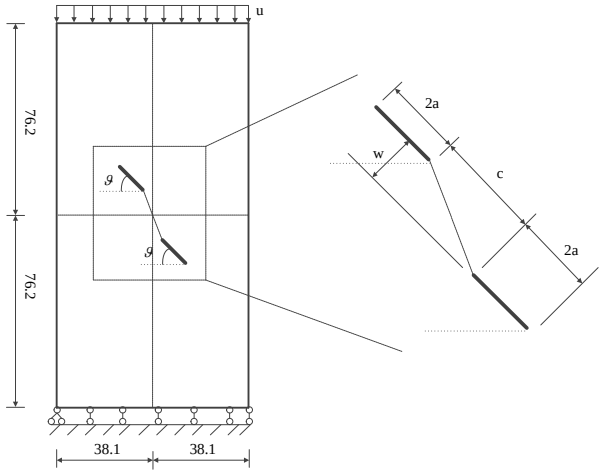

(a) Geometry and boundary conditions (b) Details

Figure 17. Rock plate with double flaws under compression (unit: mm)

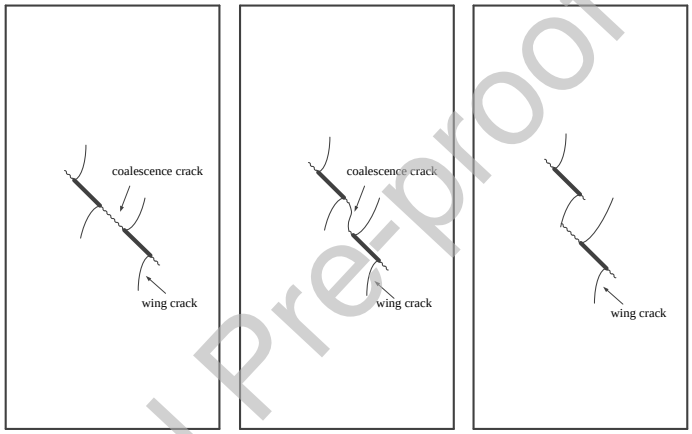

(a) 45-0-2a (b) 45-a-2a (c) 45-2a-2a

Figure 18. Crack paths in experiments for rock plates under compression

6.2.1 The case χ=0.6

Firstly, the two cases χ=0.6 with $f_c = 2.875$MPa and $f_c = 3.594$MPa are simulated to show the shear fracture and compressive-shear fracture. The crack paths for the three specimens are shown in Figure 19-Figure 24, respectively. No wing crack can be observed in all the specimens. This is because the critical shear failure stress is smaller than the critical normal failure stress, and the cracks are mainly shear fractures or compressive-shear fractures. Coalescence cracks between the two pre-existing cracks can also be observed. For the specimen "45-0-2a" with $f_c = 3.594$MPa, two coalescence cracks may be observed, especially when the length scale l_0 =0.3mm. This is because the initiation directions of the two "inner" cracks are opposite (see Figure 19(b)) and they may not be able to coalesce into one crack if the length scale is very small. The load-displacement curves are shown in Figure 25-Figure 27. The load-displacement curves show that the difference obtained by the proposed model with given softening laws (a linear

softening law in this work) is much smaller than the difference obtained by the proposed model with the classical brittle model, i.e., the length scale has a significant influence on the global responses of the specimens in the proposed model with the classical brittle model.

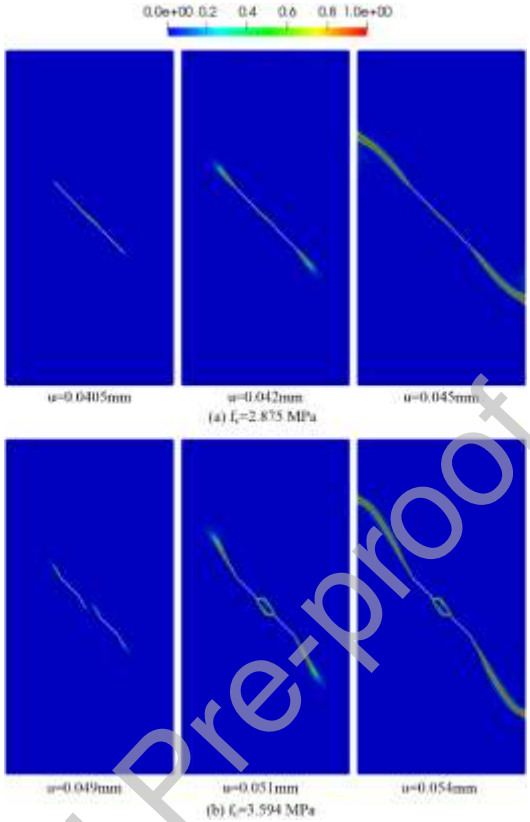

Figure 19. Crack paths for rock plate "45-0-2a" under compression (χ=0.6, linear softening model l_0=0.3mm)

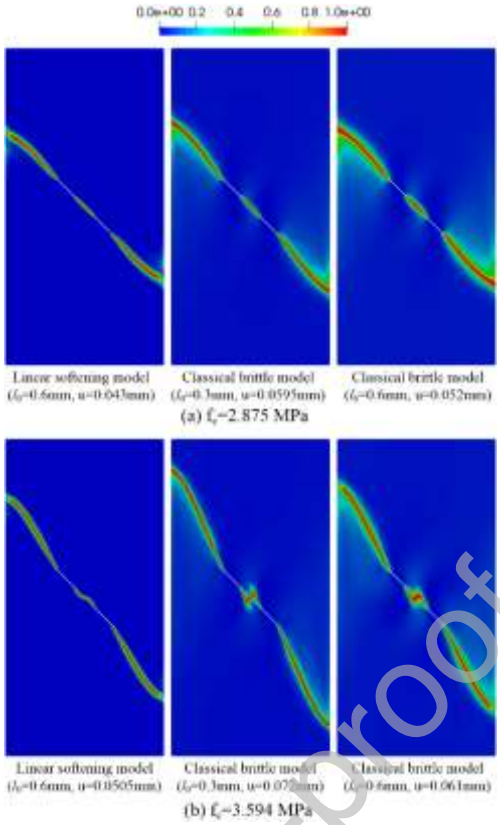

Figure 20. Crack paths for rock plate "45-0-2a" under compression (χ=0.6)

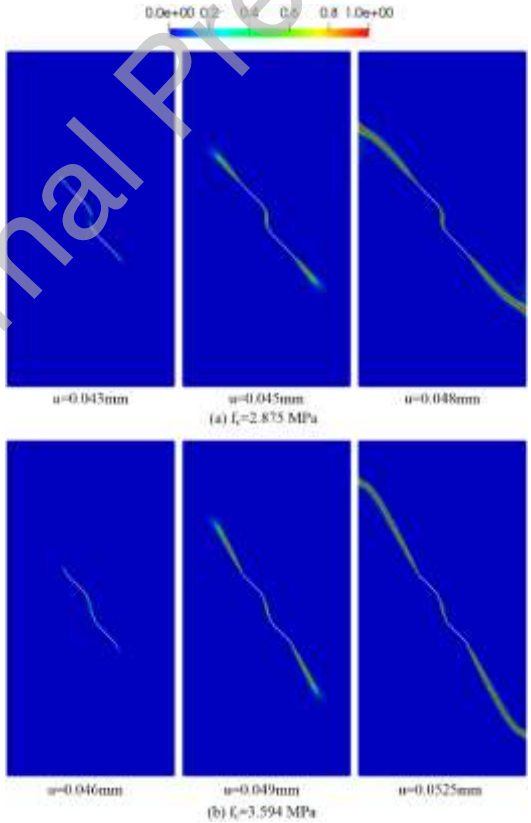

Figure 21. Crack paths for rock plate "45-a-2a" under compression (χ=0.6, linear softening model l_0=0.3mm)

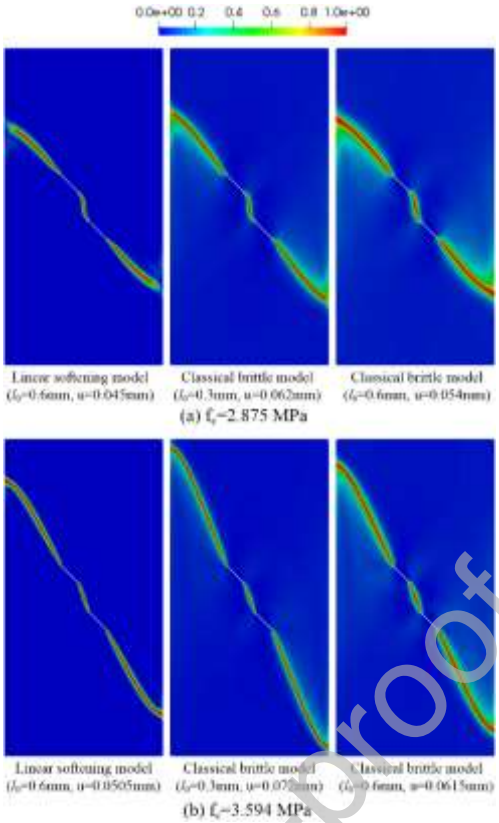

Figure 22. Crack paths for rock plate "45-a-2a" under compression (χ=0.6)

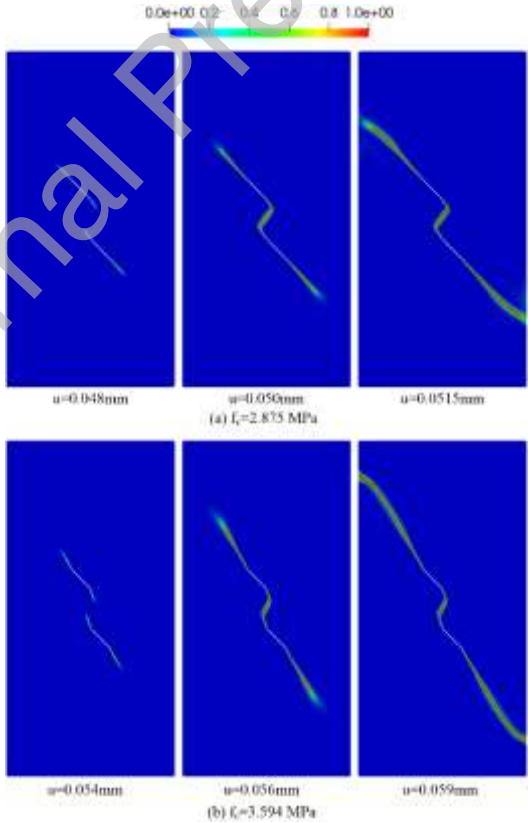

Figure 23. Crack paths for rock plate "45-2a-2a" under compression (χ=0.6, linear softening model l_0=0.3mm)

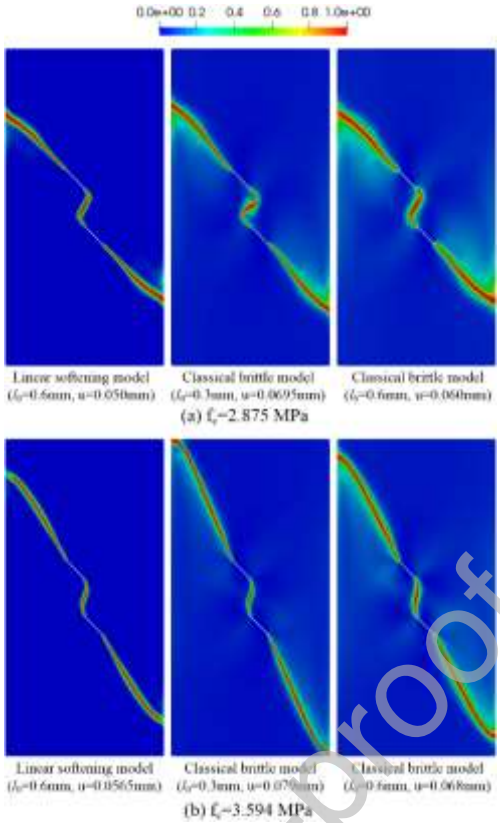

Figure 24. Crack paths for rock plate "45-2a-2a" under compression (χ=0.6)

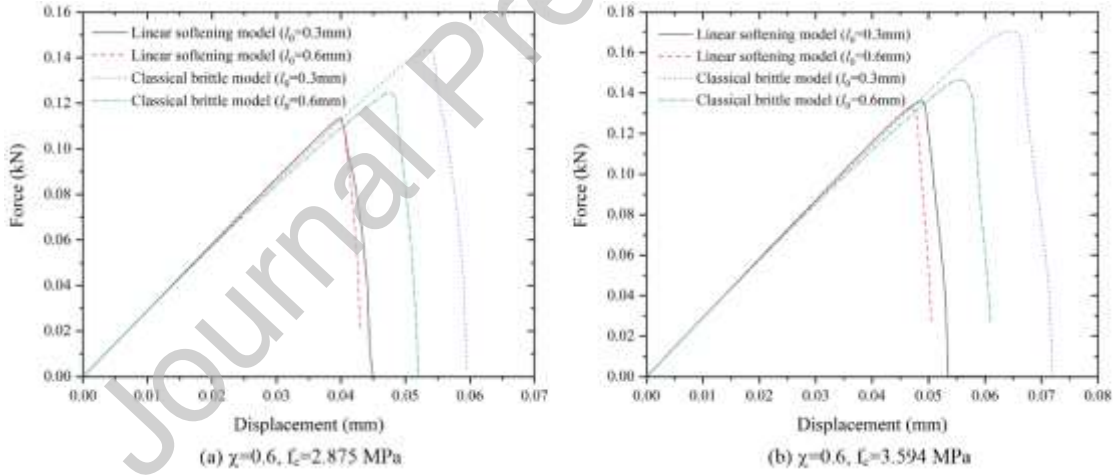

Figure 25. Load-displacement curves for rock plates with double notches under compression (χ=0.6, specimen "45-0-2a")

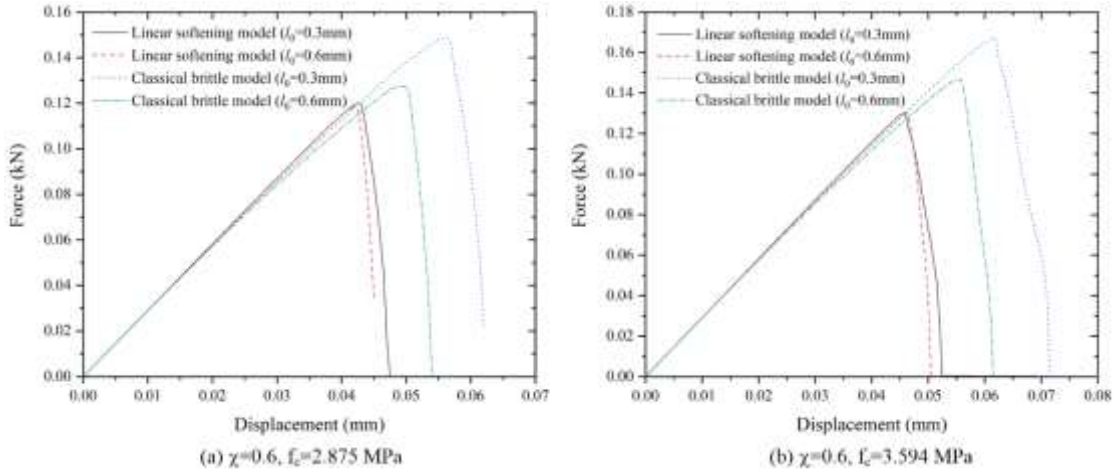

Figure 26. Load-displacement curves for rock plates with double notches under compression (χ=0.6, specimen "45-a-2a")

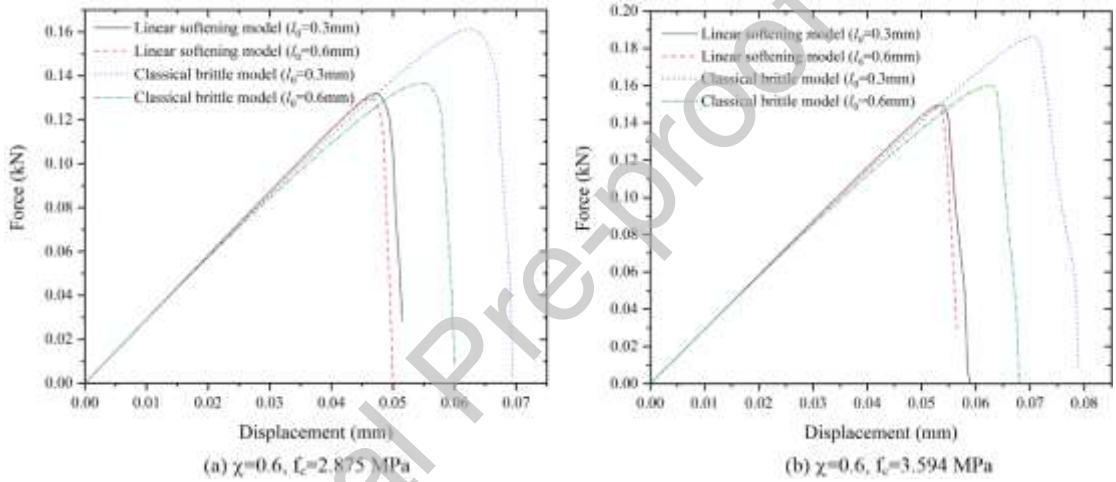

Figure 27. Load-displacement curves for rock plates with double notches under compression (χ=0.6, specimen "45-2a-2a")

6.2.2 The case χ=3.0

Secondly, the cases χ=3.0 with $f_c = 13.8$ MPa and $f_c = 16.1$ MPa are simulated to show both tension-shear and compression-shear fractures. The corresponding crack paths are shown in Figure 28-Figure 33. Good agreement between the numerical results and the experiment results [77-79] can be observed in all the specimens. Four wing cracks appear and grow first, then shear cracks or compression-shear cracks emerge and finally grow into coalescence cracks. The mode of coalescence for the three specimens may be different, and it can be either "shearing" or "shearing+tension" [77]. The load-displacement curves are shown in Figure 34-Figure 36. One can observe again that the length scale has much less influence on the global responses of the structures if the linear softening law is used in the proposed model.

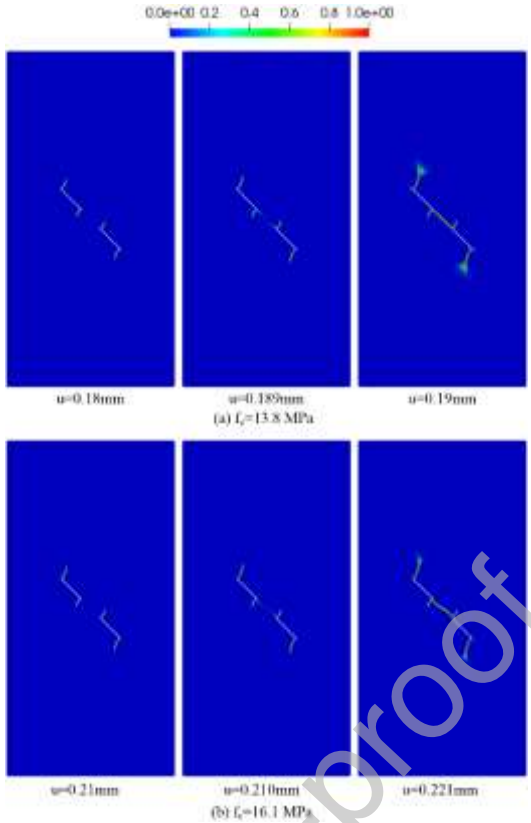

Figure 28. Crack paths for rock plate "45-0-2a" under compression (χ=3.0, linear softening model l_0=0.3mm)

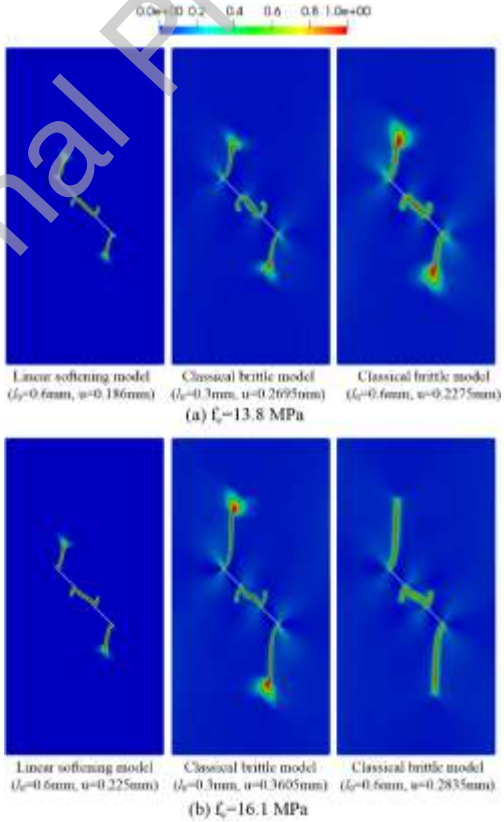

Figure 29. Crack paths for rock plate "45-0-2a" under compression (χ=3.0)

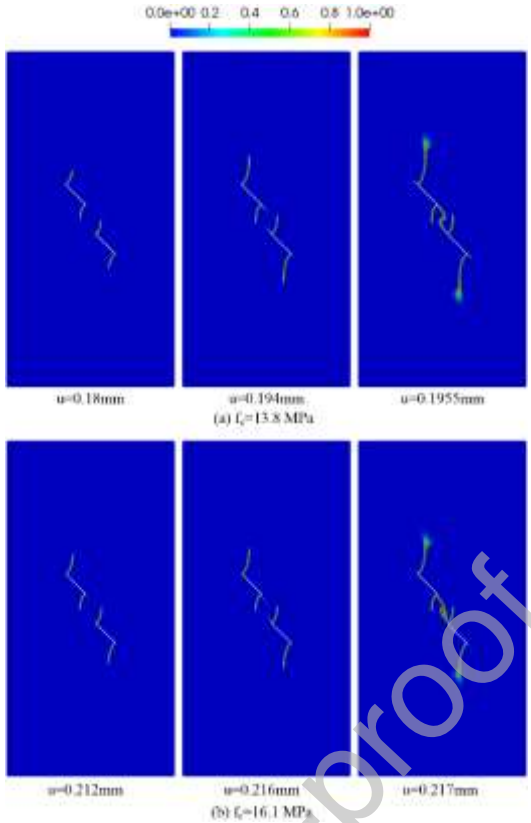

Figure 30. Crack paths for rock plate "45-a-2a" under compression (χ=3.0, linear softening model l_0=0.3mm)

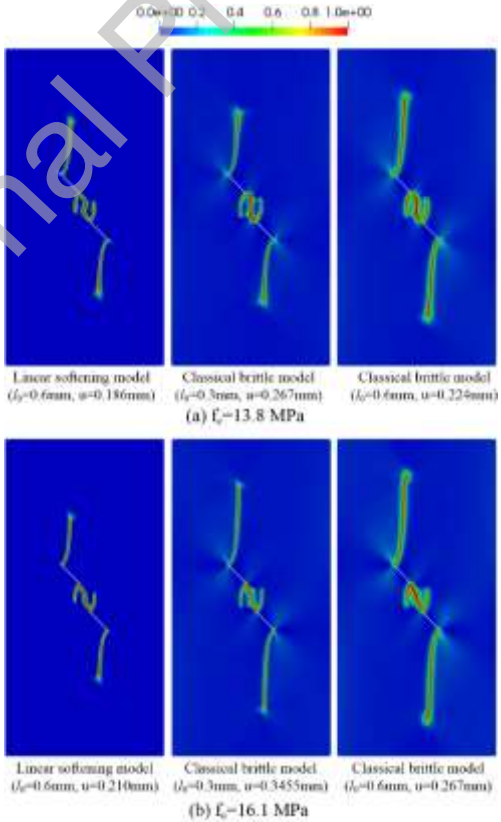

Figure 31. Crack paths for rock plate "45-a-2a" under compression (χ=3.0)

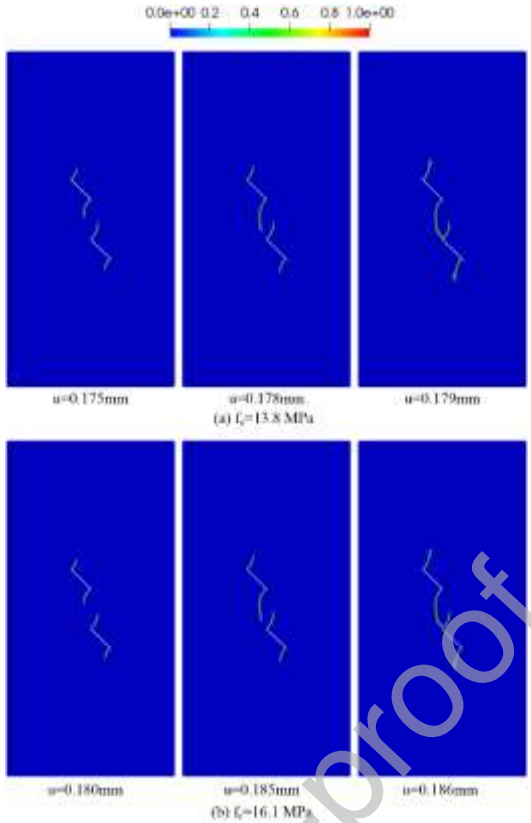

Figure 32. Crack paths for rock plate "45-2a-2a" under compression (χ=3.0, linear softening model l_0=0.3mm)

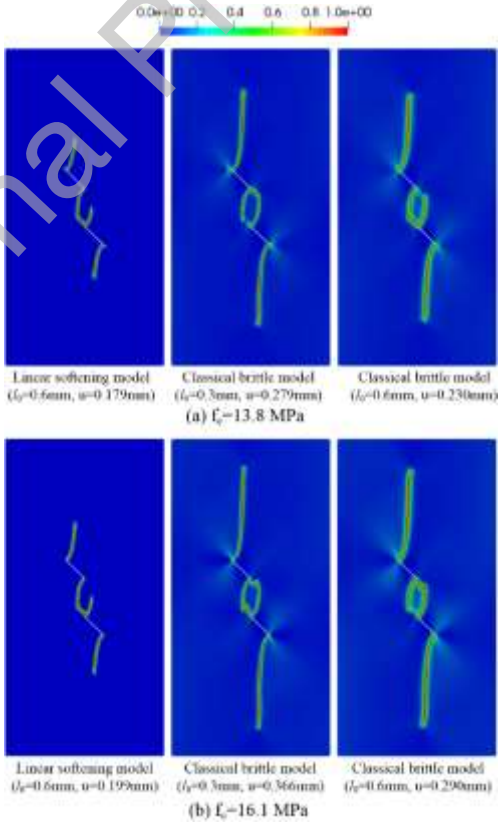

Figure 33. Crack paths for rock plate "45-2a-2a" under compression (χ=3.0)

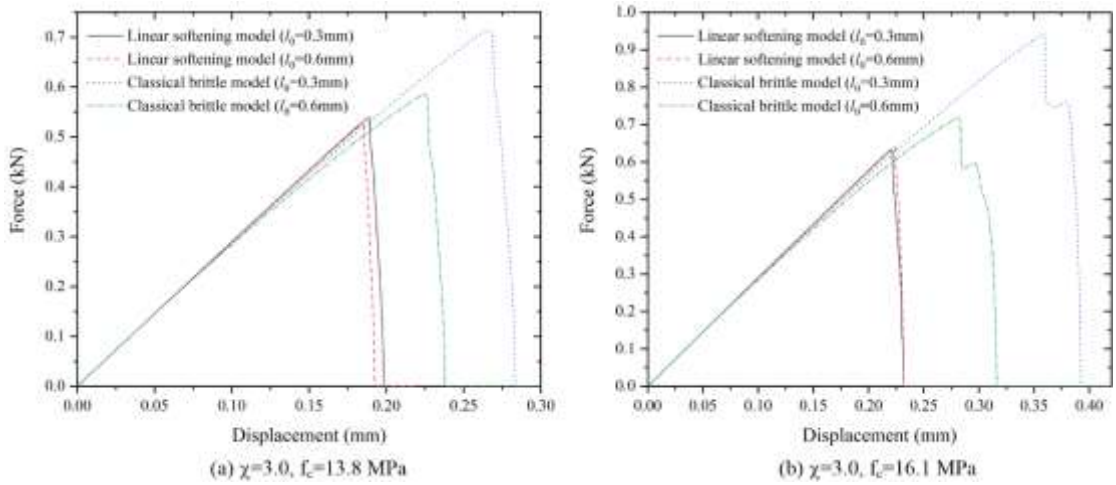

Figure 34. Load-displacement curves for rock plates with double notches under compression (χ=3.0, specimen "45-0-2a")

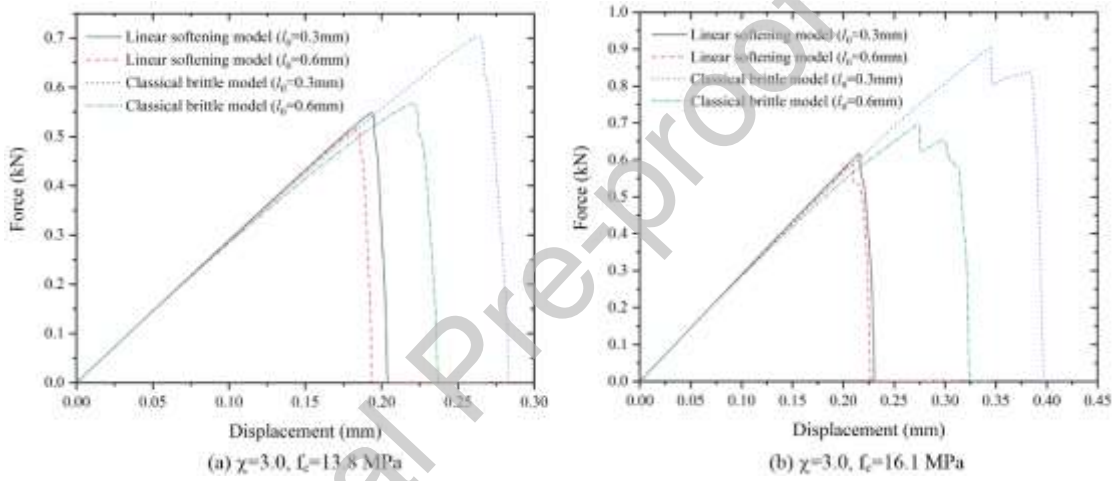

Figure 35. Load-displacement curves for rock plates with double notches under compression (χ=3.0, specimen "45-a-2a")

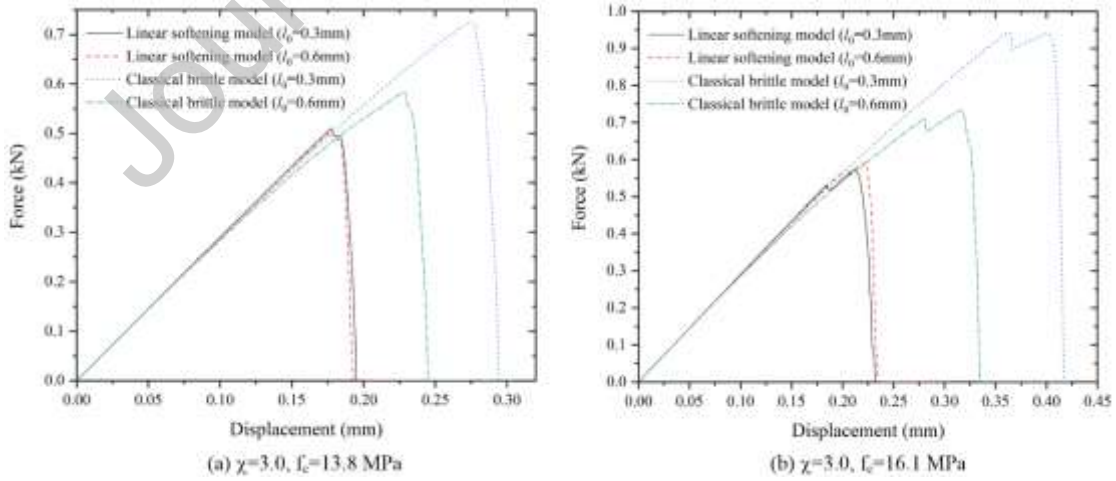

Figure 36. Load-displacement curves for rock plates with double notches under compression (χ=3.0, specimen "45-2a-2a")

7. Conclusion

In this paper, a unified phase-field model has been proposed to simulate both tensional-shear and compressive-shear fractures. The proposed model is based on the use of a universal fracture criterion, that can predict both tensional-shear and compressive-shear fractures under complex stress states and directly determine the crack direction. To consider tensional-shear and compressive-shear fractures, the strain energy of undamaged configuration is decomposed into three parts: the tensional/compressive part, the shear part, and the rest. The tensional/compressive and shear parts can be degraded by the same or different degradation functions.

The proposed model is derived from the original unified phase-field theory, and therefore, general softening laws for cohesive fracture models can also be incorporated. Numerical results have shown that the proposed model has the ability to simulate both tensional-shear and compressive-shear fractures and the results have good agreements with the experiments. Besides, the length scale has much less influence on the global response if cohesive fracture models with general softening laws are used.

Compared with the mixed model proposed by Wang et al. [55], only one additional material parameter, the failure compression strength, is needed. The proposed phase-field model can be extended to 3D cases and dynamic fractures. Applying other fracture criteria [80-82] in the model is also possible. Physical experiments will be done to validate the proposed model. The thermodynamic consistency is not satisfied in the proposed model, which will be studied in future work [31, 48, 67].

Acknowledgments

Financial support for the project from the National Key R&D Program of China (No. 2022YFC3005504) and National Natural Science Foundation of China (No. 51979207, No. 51609181, No. U2040223) is acknowledged.

References

[1] B.M. Sundaram and H.V. Tippur, *Dynamic fracture of soda-lime glass: A full-field optical investigation of crack initiation, propagation and branching,* Journal of the Mechanics and Physics of Solids. 120 (2018) 132-153.

[2] T. Rahmaan, A. Abedini, C. Butcher, N. Pathak, and M.J. Worswick, *Investigation into the shear stress, localization and fracture behaviour of DP600 and AA5182-O sheet metal alloys under elevated strain rates,* International Journal of Impact Engineering. 108 (2017) 303-321.

[3] D. Li and F. Du, *Monitoring and evaluating the failure behavior of ice structure using the acoustic emission technique,* Cold Regions Science and Technology. 129 (2016) 51-59.

[4] X. Chen, J. Bu, W. Zhou, and Q. Wang, *Effect of pre-cyclic damage and high temperature on residual tensile behavior of concrete,* Fire Safety Journal. 108 (2019) 102853.

[5] M.R.M. Aliha and A. Bahmani, *Rock Fracture Toughness Study Under Mixed Mode I/III Loading,* Rock Mechanics and Rock Engineering. 50 (7) (2017) 1739-1751.

[6] T. Cruse, *Boundary-Integral Equation Method for Three-Dimensional Elastic Fracture Mechanics Analysis*, 1975, PRATT AND WHITNEY AIRCRAFT EAST HARTFORD CONN.

[7] W. Zhou, B. Liu, Q. Wang, X. Chang, and X. Chen, *Formulations of displacement discontinuity method for crack problems based on boundary element method,* Engineering Analysis with Boundary Elements. 115 (2020) 86-95.

[8] G. Xie, F. Zhou, D. Zhang, X. Wen, and H. Li, *A novel triangular boundary crack front element for 3D crack problems based on 8-node serendipity element,* Engineering Analysis with Boundary Elements. 105 (2019) 296-302.

[9] G. Zi and T. Belytschko, *New crack‐tip elements for XFEM and applications to cohesive cracks,* International Journal for Numerical Methods in Engineering. 57 (15) (2003) 2221-2240.

[10] S.Z. Feng and X. Han, *A novel multi-grid based reanalysis approach for efficient prediction of fatigue crack propagation,* Computer Methods in Applied Mechanics and Engineering. 353 (2019) 107-122.

[11] T. Belytschko, L. Gu, and Y. Lu, *Fracture and crack growth by element free Galerkin methods,* Modelling and Simulation in Materials Science and Engineering. 2 (3A) (1994) 519.

[12] H. Ren, X. Zhuang, and T. Rabczuk, *Dual-horizon peridynamics: A stable solution to varying horizons,* Computer Methods in Applied Mechanics and Engineering. 318 (2017) 762-782.

[13] H. Ren, X. Zhuang, Y. Cai, and T. Rabczuk, *Dual-horizon Peridynamics,* International Journal for Numerical Methods in Engineering. 108 (12) (2016) 1451-1476.

[14] Y. Wang, X. Zhou, and M. Kou, *An improved coupled thermo-mechanic bond-based peridynamic model for cracking behaviors in brittle solids subjected to thermal shocks,* European Journal of Mechanics - A/Solids. 73 (2019) 282-305.

[15] T. Rabczuk, G. Zi, S. Bordas, and H. Nguyen-Xuan, *A simple and robust three-dimensional cracking-particle method without enrichment,* Computer Methods in Applied Mechanics & Engineering. 199 (37) (2010) 2437-2455.

[16] T. Rabczuk and T. Belytschko, *Cracking particles: A simplified meshfree method for arbitrary evolving cracks,* International Journal for Numerical Methods in Engineering. 61 (13) (2010) 2316-2343.

[17] P. Areias, J. Reinoso, P.P. Camanho, J.C.D. Sá, and T. Rabczuk, *Effective 2D and 3D crack propagation with local mesh refinement and the screened Poisson equation,* Engineering Fracture Mechanics. 189 (2017) S0013794417307804.

[18] P. Areias, M.A. Msekh, and T. Rabczuk, *Damage and fracture algorithm using the screened Poisson equation and local remeshing,* Engineering Fracture Mechanics. 158 (2016) 116-143.

[19] F. Yan, X.T. Feng, J.H. Lv, P.Z. Pan, and S.J. Li, *Continuous-discontinuous cellular automaton method for cohesive crack growth in rock,* Engineering Fracture Mechanics. 188 (2017) S0013794417306276.

[20] F. Yan, P. Pan, X. Feng, S. Li, and Q. Jiang, *A novel fast overrelaxation updating method for continuous-discontinuous cellular automaton,* Applied Mathematical Modelling. 66 (2019) 156-174.

[21] M. Hofacker and C. Miehe, *Continuum phase field modeling of dynamic fracture: variational principles and staggered FE implementation,* International Journal of Fracture. 178 (1-2) (2012) 113-129.

[22] J.Y. Wu, V.P. Nguyen, C.T. Nguyen, D. Sutula, S. Bordas, and S. Sinaie, *Phase field modeling of fracture,* Advances in Applied Mechancis: Multi-scale Theory and Computation. 53 (2019).

[23] X. Zhang, C. Vignes, S.W. Sloan, and D. Sheng, *Numerical evaluation of the phase-field model for brittle fracture with emphasis on the length scale,* Computational Mechanics. 59 (5) (2017) 737-752.

[24] S. Zhou, X. Zhuang, H. Zhu, and T. Rabczuk, *Phase field modelling of crack propagation, branching and coalescence in rocks,* Theoretical and Applied Fracture Mechanics. 96 (2018) 174-192.

[25] I. Aranson, V. Kalatsky, and V. Vinokur, *Continuum field description of crack propagation,* Physical Review Letters. 85 (1) (2000) 118.

[26] A. Karma, D.A. Kessler, and H. Levine, *Phase-field model of mode III dynamic fracture,* Physical Review Letters. 87 (4) (2001) 045501.

[27] V. Hakim and A. Karma, *Laws of crack motion and phase-field models of fracture,* Journal of the Mechanics and Physics of Solids. 57 (2) (2009) 342-368.

[28] R. Spatschek, E. Brener, and A. Karma, *Phase field modeling of crack propagation,* Philosophical Magazine. 91 (1) (2011) 75-95.

[29] H. Henry and H. Levine, *Dynamic instabilities of fracture under biaxial strain using a phase field model,* Physical review letters. 93 (10) (2004) 105504.

[30] C.-H. Chen, E. Bouchbinder, and A. Karma, *Instability in dynamic fracture and the failure of the classical theory of cracks,* Nature Physics. 13 (12) (2017) 1186.

[31] H. Amor, J.-J. Marigo, and C. Maurini, *Regularized formulation of the variational brittle fracture with unilateral contact: Numerical experiments,* Journal of the Mechanics and Physics of Solids. 57 (8) (2009) 1209-1229.

[32] C. Kuhn and R. Müller, *A continuum phase field model for fracture,* Engineering Fracture Mechanics. 77 (18) (2010) 3625-3634.

[33] G.A. Francfort and J.-J. Marigo, *Revisiting brittle fracture as an energy minimization problem,* Journal of the Mechanics and Physics of Solids. 46 (8) (1998) 1319-1342.

[34] B. Bourdin, G.A. Francfort, and J.-J. Marigo, *Numerical experiments in revisited brittle fracture,* Journal of the Mechanics and Physics of Solids. 48 (4) (2000) 797-826.

[35] C.J. Larsen, C. Ortner, and E. Süli, *Existence of solutions to a regularized model of dynamic fracture,* Mathematical Models and Methods in Applied Sciences. 20 (07) (2010) 1021-1048.

[36] B. Bourdin, C.J. Larsen, and C.L. Richardson, *A time-discrete model for dynamic fracture based on crack regularization,* International journal of fracture. 168 (2) (2011) 133-143.

[37] M.J. Borden, C.V. Verhoosel, M.A. Scott, T.J. Hughes, and C.M. Landis, *A phase-field description of dynamic brittle fracture,* Computer Methods in Applied Mechanics and Engineering. 217 (2012) 77-95.

[38] M. Hofacker and C. Miehe, *A phase field model of dynamic fracture: Robust field updates for the analysis of complex crack patterns,* International Journal for Numerical Methods in Engineering. 93 (3) (2013) 276-301.

[39] A. Schlüter, A. Willenbücher, C. Kuhn, and R. Müller, *Phase field approximation of dynamic brittle fracture,* Computational Mechanics. 54 (5) (2014) 1141-1161.

[40] H.L. Ren, X.Y. Zhuang, C. Anitescu, and T. Rabczuk, *An explicit phase field method for brittle dynamic fracture,* Computers & Structures. 217 (2019) 45-56.

[41] F. Amiri, D. Millán, Y. Shen, T. Rabczuk, and M. Arroyo, *Phase-field modeling of fracture in linear thin shells,* Theoretical and Applied Fracture Mechanics. 69 (2014) 102-109.

[42] P. Areias, T. Rabczuk, and M.A. Msekh, *Phase-field analysis of finite-strain plates and shells including element subdivision,* Computer Methods in Applied Mechanics and Engineering. 312 (2016) 322-350.

[43] M.A. Msekh, N.H. Cuong, G. Zi, P. Areias, X. Zhuang, and T. Rabczuk, *Fracture properties prediction of clay/epoxy nanocomposites with interphase zones using a phase field model,* Engineering Fracture Mechanics. 188 (2018) 287-299.

[44] D. Chu, X. Li, Z. Liu, J. Cheng, T. Wang, Z. Li, and Z. Zhuang, *A unified phase field damage model for modeling the brittle-ductile dynamic failure mode transition in metals,* Engineering Fracture Mechanics. 212 (2019) 197-209.

[45] B. Chen, Y. Sun, B.R. Barboza, A.R. Barron, and C. Li, *Phase-field simulation of hydraulic fracturing with a revised fluid model and hybrid solver,* Engineering Fracture Mechanics. 229 (2020) 106928.

[46] M. Ambati, T. Gerasimov, and L. De Lorenzis, *A review on phase-field models of brittle fracture and a new fast hybrid formulation,* Computational Mechanics. 55 (2) (2015) 383-405.

[47] C. Miehe, M. Hofacker, and F. Welschinger, *A phase field model for rate-independent crack propagation: Robust algorithmic implementation based on operator splits,* Computer Methods in Applied Mechanics and Engineering. 199 (45) (2010) 2765-2778.

[48] C. Miehe, F. Welschinger, and M. Hofacker, *Thermodynamically consistent phase‐field models of fracture: Variational principles and multi‐field FE implementations,* International Journal for Numerical Methods in Engineering. 83 (10) (2010) 1273-1311.

[49] J.Y. Wu, V.P. Nguyen, H. Zhou, and Y. Huang, *A variationally consistent phase-field anisotropic damage model for fracture,* Computer Methods in Applied Mechanics and Engineering. 358 (2020) 112629.

[50] J.Y. Wu and M. Cervera, *A novel positive/negative projection in energy norm for the damage modeling of quasi-brittle solids,* International Journal of Solids and Structures. 139-140 (2018) 250-269.

[51] C. Steinke and M. Kaliske, *A phase-field crack model based on directional stress decomposition,* Computational Mechanics. 63 (5) (2019) 1019-1046.

[52] X. Zhang, S.W. Sloan, C. Vignes, and D. Sheng, *A modification of the phase-field model for mixed mode crack propagation in rock-like materials,* Computer Methods in Applied Mechanics and Engineering. 322 (2017) 123-136.

[53] B. Shen and O. Stephansson, *Modification of the G-criterion for crack propagation subjected to compression,* Engineering Fracture Mechanics. 47 (2) (1994) 177-189.

[54] E.C. Bryant and W. Sun, *A mixed-mode phase field fracture model in anisotropic rocks with consistent kinematics,* Computer Methods in Applied Mechanics and Engineering. 342 (2018) 561-584.

[55] Q. Wang, Y.T. Feng, W. Zhou, Y. Cheng, and G. Ma, *A phase-field model for mixed-mode fracture based on a unified tensile fracture criterion,* Computer Methods in Applied Mechanics and Engineering. 370 (2020) 113270.

[56] S. Zhou, X. Zhuang, and T. Rabczuk, *Phase field modeling of brittle compressive-shear*

fractures in rock-like materials: A new driving force and a hybrid formulation, Computer Methods in Applied Mechanics and Engineering. 355 (2019) 729-752.

[57] T. Wang, X. Ye, Z. Liu, D. Chu, and Z. Zhuang, *Modeling the dynamic and quasi-static compression-shear failure of brittle materials by explicit phase field method,* Computational Mechanics. 64 (6) (2019) 1537-1556.

[58] R.T. Qu and Z.F. Zhang, *A universal fracture criterion for high-strength materials,* Scientific reports. 3 (2013) 1117.

[59] J.Y. Wu, *A unified phase-field theory for the mechanics of damage and quasi-brittle failure,* Journal of the Mechanics and Physics of Solids. 103 (2017) 72-99.

[60] B. Bourdin, G.A. Francfort, and J.-J. Marigo, *The variational approach to fracture,* Journal of elasticity. 91 (1-3) (2008) 5-148.

[61] K.M. Hamdia, M. Silani, X. Zhuang, P. He, and T. Rabczuk, *Stochastic analysis of the fracture toughness of polymeric nanoparticle composites using polynomial chaos expansions,* International Journal of Fracture. 206 (3) (2017) 1-13.

[62] C. Kuhn, A. Schlüter, and R. Müller, *On degradation functions in phase field fracture models,* Computational Materials Science. 108 (2015) 374-384.

[63] K. Pham, H. Amor, J.-J. Marigo, and C. Maurini, *Gradient damage models and their use to approximate brittle fracture,* International Journal of Damage Mechanics. 20 (4) (2011) 618-652.

[64] B. Bourdin, J.-J. Marigo, C. Maurini, and P. Sicsic, *Morphogenesis and propagation of complex cracks induced by thermal shocks,* Physical review letters. 112 (1) (2014) 014301.

[65] E. Lorentz and V. Godard, *Gradient damage models: Toward full-scale computations,* Computer Methods in Applied Mechanics and Engineering. 200 (21) (2011) 1927-1944.

[66] Q. Wang, W. Zhou, and Y.T. Feng, *The phase-field model with an auto-calibrated degradation function based on general softening laws for cohesive fracture,* Applied Mathematical Modelling. 86 (2020) 185-206.

[67] S. Liu, Y. Wang, C. Peng, and W. Wu, *A thermodynamically consistent phase field model for mixed-mode fracture in rock-like materials,* Computer Methods in Applied Mechanics and Engineering. 392 (2022) 114642.

[68] Z. Zhang and J. Eckert, *Unified tensile fracture criterion,* Physical review letters. 94 (9) (2005) 094301.

[69] J.Y. Wu, *Robust numerical implementation of non-standard phase-field damage models for failure in solids,* Computer Methods in Applied Mechanics and Engineering. (2018).

[70] S.J. Benson and T.S. Munson, *Flexible complementarity solvers for large-scale applications,* Optimization Methods and Software. 21 (1) (2006) 155-168.

[71] A.R. Ingraffea and F.E. Heuze, *Finite element models for rock fracture mechanics,* International Journal for Numerical and Analytical Methods in Geomechanics. 4 (1) (1980) 25-43.

[72] L.N.Y. Wong and H.H. Einstein, *Systematic evaluation of cracking behavior in specimens containing single flaws under uniaxial compression,* International Journal of Rock Mechanics and Mining Sciences. 46 (2) (2009) 239-249.

[73] E.Z. Lajtai, *Brittle fracture in compression,* International Journal of Fracture. 10 (4) (1974) 525-536.

[74] S.-Q. Yang and H.-W. Jing, *Strength failure and crack coalescence behavior of brittle sandstone*

samples containing a single fissure under uniaxial compression, International Journal of Fracture. 168 (2) (2011) 227-250.

[75] Y.-P. Li, L.-Z. Chen, and Y.-H. Wang, *Experimental research on pre-cracked marble under compression,* International Journal of Solids and Structures. 42 (9) (2005) 2505-2516.

[76] J.Y. Wu and V.P. Nguyen, *A length scale insensitive phase-field damage model for brittle fracture,* Journal of the Mechanics and Physics of Solids. 119 (2018) 20-42.

[77] A. Bobet and H.H. Einstein, *Numerical modeling of fracture coalescence in a model rock material,* International Journal of Fracture. 92 (3) (1998) 221-252.

[78] B. Shen, *The mechanism of fracture coalescence in compression—experimental study and numerical simulation,* Engineering Fracture Mechanics. 51 (1) (1995) 73-85.

[79] R.H.C. Wong, K.T. Chau, C.A. Tang, and P. Lin, *Analysis of crack coalescence in rock-like materials containing three flaws—Part I: experimental approach,* International Journal of Rock Mechanics and Mining Sciences. 38 (7) (2001) 909-924.

[80] J.Y. Wu and M. Cervera, *On the equivalence between traction- and stress-based approaches for the modeling of localized failure in solids,* Journal of the Mechanics and Physics of Solids. 82 (2015) 137-163.

[81] M. Cervera and J.-Y. Wu, *On the conformity of strong, regularized, embedded and smeared discontinuity approaches for the modeling of localized failure in solids,* International Journal of Solids and Structures. 71 (2015) 19-38.

[82] J.Y. Wu and M. Cervera, *A thermodynamically consistent plastic-damage framework for localized failure in quasi-brittle solids: Material model and strain localization analysis,* International Journal of Solids and Structures. 88-89 (2016) 227-247.